Eidgenössische Technische Hochschule Zürich
Swiss Federal Institute of Technology Zurich

UNIVERSITY OF OXFORD

Master Thesis

Vibrations of Ultralight Tracking Detector Structures

Mu3e Collaboration

Spring Term 2025

Supervised by:
Prof. Dr. Daniela Bortoletto
Prof. Dr. Rainer Wallny
Dr. Ashley McDougall
Dr. Georg Viehhauser

Author:
Mattia Moretti

Abstract

This thesis investigates the vibrational behaviour of silicon pixel detectors used in the Mu3e experiment, compares alternative design configurations through experiments and simulations, and evaluates whether further mechanical reinforcement is required. Vibrational responses were measured using a shaker table, and theoretical models were established to fit the linear response functions. These models were then combined with measured background motion at the experimental site, using the Wiener-Khinchin theorem, to estimate the expected Root Mean Squared (RMS) displacement during operation. An additional airflow test supported by computational fluid dynamics simulations was conducted to assess performance under operational cooling conditions. The RMS displacement at the centre of a single Layer 4 ladder due to background motion was found to be $x_{\mathrm{RMS}} < 3\,\mu\mathrm{m}$, while vibrations induced by gaseous cooling flow are expected to remain at $x_{\mathrm{RMS}} < 21\,\mu\mathrm{m}$. The latter estimate should be interpreted with caution, as it is derived from a comparison between wind tunnel measurements at the University of Oxford and the helium cooling system employed in the experiment. The two setups likely differ in flow regime, with the operational flow expected to be more laminar. As these values are smaller than the pixel resolution, detector performance remains limited by multiple Coulomb scattering. Consequently, no significant degradation due to vibrations is expected, and no further mechanical stability measures are deemed necessary.

Contents

Introduction

The Standard Model (SM) of particle physics stands as one of the most successful theoretical models in modern science, offering a combined quantum description of the electromagnetic, weak, and strong interactions. Its theoretical predictions have been validated experimentally with remarkable precision [1]. Despite this, a number of open questions and observed discrepancies indicate that it is not a complete theory. Given its high accuracy, probing properties of the SM in extreme regimes requires carefully engineered experiments capable of delivering the accuracy necessary to reveal potential signs of physics beyond the Standard Model.

The Mu3e experiment is designed to be one such probe, aiming to improve the current experimental bounds on the branching ratio of the charged lepton flavour violating decay of an anti-muon into two positrons and one electron. Within the SM (including neutrino mixing), this decay is highly suppressed, with a predicted branching ratio below 10^{-53} [2]. Any observation of this decay in the experiment would therefore constitute clear evidence for new physics [3]. Before decaying, muons are brought to rest; therefore, the resulting electrons and positrons have momenta below 53 MeV/c. In this regime, multiple Coulomb scattering dominates the track resolution, making an ultralight detector volume essential for achieving Mu3e's physics goals. The detector elements constructed under these stringent requirements are known as ladders, a term inspired by their elongated, lightweight structure. Each ladder consists of ultrathin silicon pixel sensors mounted on flexible support structures, designed to minimise material while preserving mechanical integrity. To further enhance stability and suppress unwanted deformations, the ladders are reinforced with carbon-fibre stiffeners. Despite these measures, the delicate design means that ladders are susceptible to vibrational motion, which, while not expected to be the dominant source of uncertainty, can still impact the tracking performance.

The objective of this thesis is to study the vibrational response of ladders from the outermost detector layer to excitations from both background motion and helium cooling flow. A number of ladders were tested using a shaker table and a wind tunnel. Using experimental measurements and simulations conducted at the University of Oxford, together with data collected at the future experimental site and computational fluid dynamics (CFD) simulations of the helium cooling system, an upper limit for the standard deviation of ladder displacement was determined and evaluated in the context of the detector's resolution requirements.

This thesis is structured in the following way. Chapter 1 provides the scientific context, including an overview of the SM and the Mu3e experiment. Chapter 2 introduces the key mechanics concepts applied throughout the analysis. Chapter 3 presents shaker table measurements and examines the vibrational effects of the helium compressors, while Chapter 4 focuses on flow-induced vibrations. Finally, the results are summarised and placed in a broader context in Chapter 5.

Chapter 1

Scientific context and the Mu3e experiment

1.1 The Standard Model of particle physics

The SM of particle physics is a relativistic quantum field theory that describes all known fundamental particles and interactions, with the exception of gravity. Its development gained momentum during the 1960s and 1970s, driven by the understanding of three key theoretical advances of the time: the quark model, the idea of local gauge symmetry, and the concept of spontaneous symmetry breaking [4].

The theory is formulated on flat Minkowski spacetime $\mathbb{R}^{1,3}$, whose symmetry group is the proper, orthochronous part of the Poincaré group, denoted by $\mathrm{ISO}^+(1,3)$ [5]. The content of the theory consists of a collection of quantised fields, whose excitations correspond to the matter particles (fermions) and force carriers (bosons), all treated as point-like. These fields are introduced through Lagrangian densities. All bosons except the Higgs arise as gauge bosons, resulting from the requirement of local gauge invariance under the product of Lie groups

$$\mathrm{SU}(3)_\mathrm{C} \times \mathrm{SU}(2)_\mathrm{L} \times \mathrm{U}(1)_\mathrm{Y}, \tag{1.1}$$

which together form the gauge group of the SM. Here,

- $\mathrm{SU}(3)_\mathrm{C}$ describes the non-Abelian symmetry of the strong interaction (quantum chromodynamics), acting on the colour degrees of freedom of quarks.
- $\mathrm{SU}(2)_\mathrm{L}$ describes the non-Abelian symmetry of the weak interaction, acting only on left-handed fermions.
- $\mathrm{U}(1)_\mathrm{Y}$ is the Abelian symmetry associated with weak hypercharge.

This gauge structure dictates the form of the interaction terms in the Lagrangian [6]. Together with the kinetic terms, the Higgs potential, and the Yukawa interactions, these gauge interactions comprise the full Lorentz invariant Lagrangian density of the SM, from which the dynamics of the theory are derived [7].

All fields in the SM are categorised as either fermions or bosons. Bosons transform under integer spin representations of the double cover of the Lorentz group $\mathrm{SO}^+(1,3)$, which is denoted by $\mathrm{SL}(2,\mathbb{C})$ [8]. Fermions transform under spin-$\frac{1}{2}$ representations of $\mathrm{SL}(2,\mathbb{C})$, reflecting their half-integer spin nature. They are grouped into leptons and quarks, depending on whether or not they experience the strong

nuclear force. The SM includes six quarks and six leptons, organised into three generations of doublets, differentiated by their masses, starting with the first generation as the lightest. A schematic overview of the particle content of the SM is shown in Figure 1.1.

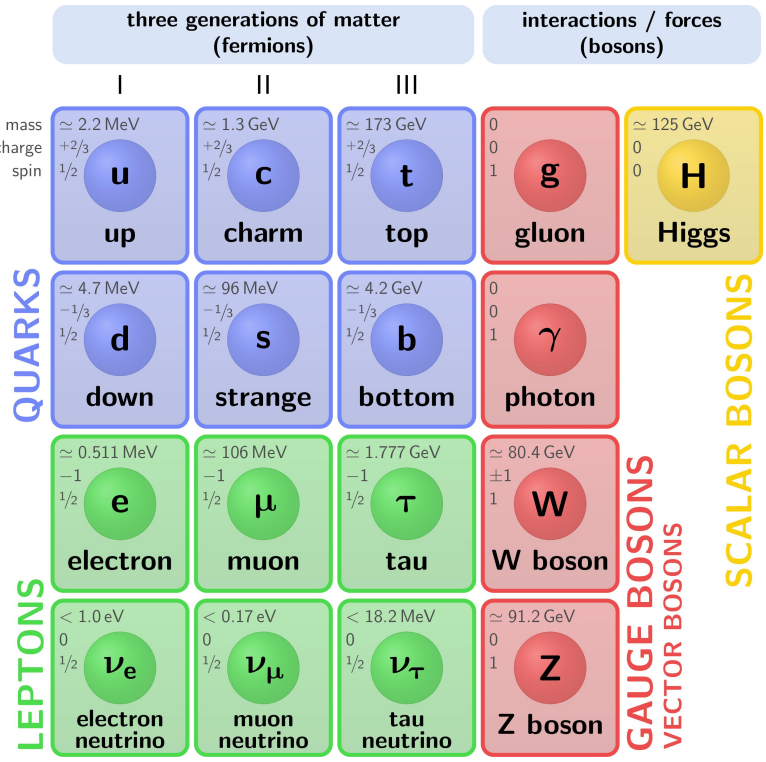

Figure 1.1: Summary of the elementary particle content of the SM [9].

Leptons possess a property known as lepton flavour. It defines which generation each lepton belongs to. For example, the presence of an electron or an electron neutrino, being leptons of the first generation, contributes L_e (electron flavour). Their corresponding antiparticles, such as the positron or electron antineutrino, contribute $-L_e$, reducing the electron flavour count by one. In the SM without neutrino oscillations, lepton flavour is a conserved quantity, meaning that there is no process that changes the lepton flavour of a given state.

1.2 Muon decay

Muons are classified as leptons of the second generation. They are unstable elementary particles and decay via the weak interaction, having a mean lifetime of approximately 2.2 µs [10]. The most common decay mode of the muon is the Michel decay, shown in Figure 1.2. Its branching ratio, the probability that this specific decay occurs when a decay takes place, is nearly 100% [1].

Lepton flavour violation (LFV) has been experimentally observed in the neutrino sector, through the phenomenon of neutrino oscillations. This observation can be accommodated in the SM by allowing neutrinos to have non-zero mass and to change flavour as they propagate [12]. To account for this, the SM must be extended to include neutrino masses and mixing. As a consequence, Standard Model extensions allow other LFV processes, specifically charged lepton flavour violating processes.

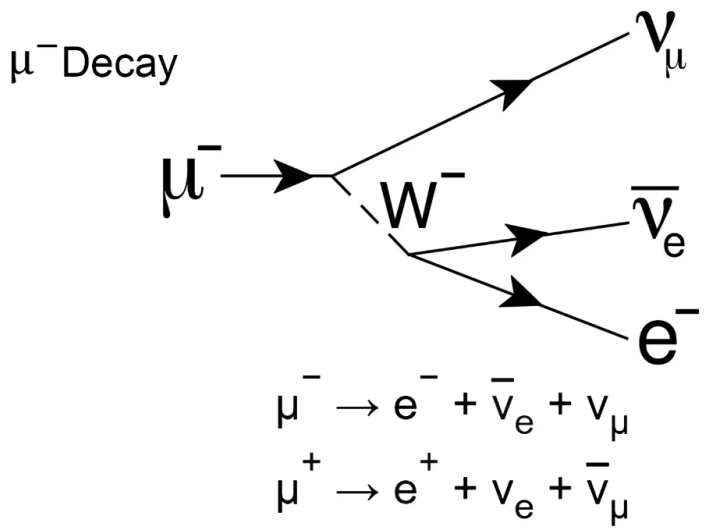

Figure 1.2: Feynman Diagram of the Michel decay of the muon [11].

Charged lepton flavour violation (cLFV) refers to processes involving a charged lepton, that violate the conservation of lepton flavour. One such cLFV process is the decay of an anti-muon into two positrons and one electron $\mu^+ \to e^+e^-e^+$. The exact rate of such processes depends on the extension Lagrangian, dictating the precise mechanism behind neutrino masses and lepton mixing [13]. For the $\mu^+ \to e^+e^-e^+$ decay, various values can be found throughout the literature, all of them below 10^{-50} [2, 3, 14]. Other theories that go beyond the SM predict the branching ratio of the Mu3e process to be much higher, rendering this decay a sensitive probe of physics beyond the SM [15].

1.3 The Mu3e experiment

The Mu3e experiment aims to detect the $\mu^+ \to e^+e^-e^+$ decay or, alternatively, to exclude a branching ratio above 10^{-16} at the 90% confidence level, thereby surpassing the precision achieved by previous experiments, such as the SINDRUM experiment, by several orders of magnitude [16].

Data taking for the Mu3e experiment is scheduled in two main phases. Phase I will be using the $\pi E5$ beam line at Paul Scherrer Institute (PSI), where up to 10^8 muons can be delivered per second. The aim is to reach a single event sensitivity of $2 \cdot 10^{-15}$, already approaching the target of 10^{-16}. Phase II will utilise the High Intensity Muon Beam (HIMB), currently under development at PSI [17], which is planned to deliver an order of magnitude more muons, enabling the experiment to reach its final sensitivity. Achieving the target sensitivity requires not only access to very high muon beam rates but also strict requirements on the experimental design. Specifically, the high rates necessitate a time resolution better than 100 ps, while efficient background suppression demands a momentum resolution below 0.5 MeV/c and a vertex resolution better than 200 µm [18].

1.4 Multiple scattering and detector resolution

In the low energy regime relevant for the Mu3e experiment, track resolution is dominated by the effects of multiple scattering rather than by the intrinsic resolution of the fine grained pixel detector. Multiple scattering refers to the deflection of charged particle trajectories as they traverse material. An illustration of how multiple scattering compares to pixel resolution in the multiple scattering dominated regime is shown in Figure 1.3.

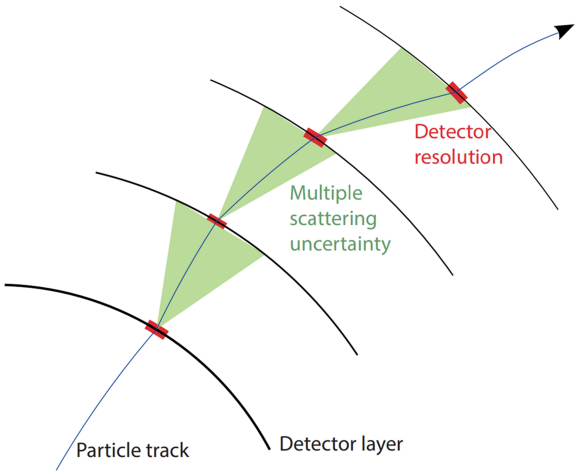

Figure 1.3: Conceptual illustration of track uncertainty due to multiple scattering and pixel size in the multiple scattering dominated regime (not to scale) [19].

A central objective of the detector design is to reduce multiple scattering and its impact on detector performance. This requirement is addressed in various ways, one of which is the application of a solenoidal magnetic field of 1 T. In this magnetic field, the momentum of charged particles is determined from the curvature of their trajectories. By selecting the magnetic field strength such that tracks re-curl within the detector acceptance, the dominant contribution to the momentum uncertainty from multiple scattering is significantly reduced, as the effect partially averages out after half a turn. This strategy is made feasible by the use of a stopping target, consisting of a hollow double-cone of thin biaxially-oriented polyethylene terephthalate foils. Incoming muons are brought to rest and subsequently decay, limiting the momentum of decay product tracks to a maximum of 53 MeV/c. Another important design measure is the minimisation of the active detector volume. Lowering the material budget reduces the fraction of a radiation length traversed by particles and thereby decreases the number of scattering events [20]. The radiation length is defined as the mean distance over which the energy of an electron is reduced to $1/e$ of its initial value through bremsstrahlung. This consideration has motivated the development and construction of an ultralight silicon tracking detector [19].

1.5 The Mu3e pixel detector

The Mu3e pixel detector consists of three main components: the central tracking station and two re-curl stations positioned on either side of it. A schematic overview

of the detector layout is shown in Figure 1.4. At the centre of the central station lies the hollow double-cone stopping target, which is surrounded by the inner vertex detector. This detector comprises two silicon pixel layers (Layer 1 and Layer 2) that deliver the essential hit information for reconstructing particle trajectories and decay vertices. Enclosing the vertex detector is the scintillating fibre (SciFi) detector, which enhances the timing resolution and assists in determining the charge of the traversing particles. The entire system is completed by two additional pixel layers (Layer 3 and Layer 4), forming the outer tracker. The re-curl stations are equipped with scintillating tiles for precision timing, as well as additional pixel layers, further extending the tracking volume. Together, these subsystems ensure that tracks curling back due to the magnetic field still intersect the detector layers and can be reconstructed, thereby increasing the overall detector acceptance.

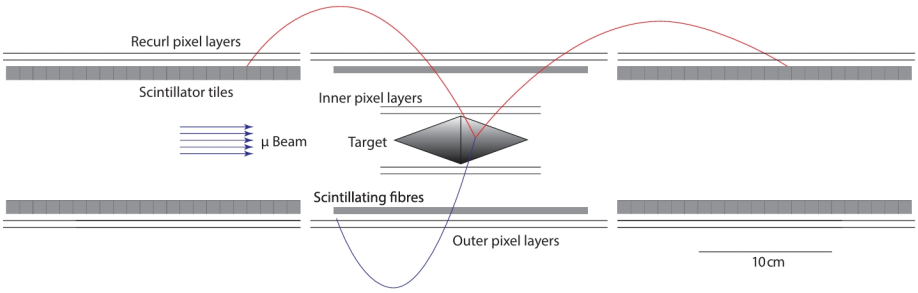

Figure 1.4: Schematic view of the Mu3e detector cut along the beam axis. The re-curl stations are located at both ends of the central station. Image adapted from internal Mu3e documentation.

A key feature of the Mu3e detector design is the use of High-Voltage Monolithic Active Pixel Sensors (HV-MAPS). These devices combine particle detection and readout within a single sensor, drastically reducing the material budget and minimising the effects of multiple scattering. The material is further reduced through the use of ultrathin MuPix sensors, specifically developed for the Mu3e experiment, which can be thinned down to a mere 50 µm for the vertex detector and 70 µm for the outer layers [21].

1.6 Helium cooling system

During operation, the power generated by the MuPix sensors must be removed. To prevent the sensors from exceeding their thermal limit of 70 °C, an efficient cooling system is essential [19]. Owing to its high specific heat capacity, more than five times greater than that of air, its low density, approximately one-seventh that of air, and its manoeuvrability, gaseous helium has been chosen as the coolant. The helium is supplied at a temperature of approximately $T_H \approx 0\,°\mathrm{C}$ and circulated through the magnet, housing the detector, using four miniature turbo compressors. The total helium flow rate of $50\,\mathrm{g\,s^{-1}}$ is distributed across several dedicated cooling circuits, that is, individual flow loops designed to remove heat from specific detector subsystems. Of this, approximately $16\,\mathrm{g\,s^{-1}}$ is directed to the regions between layers 3 and 4, cooling more than 900 silicon sensors, while approximately $2\,\mathrm{g\,s^{-1}}$ is supplied to the vertex detector. A flow diagram of the helium cooling infrastructure is shown in Figure 1.5.

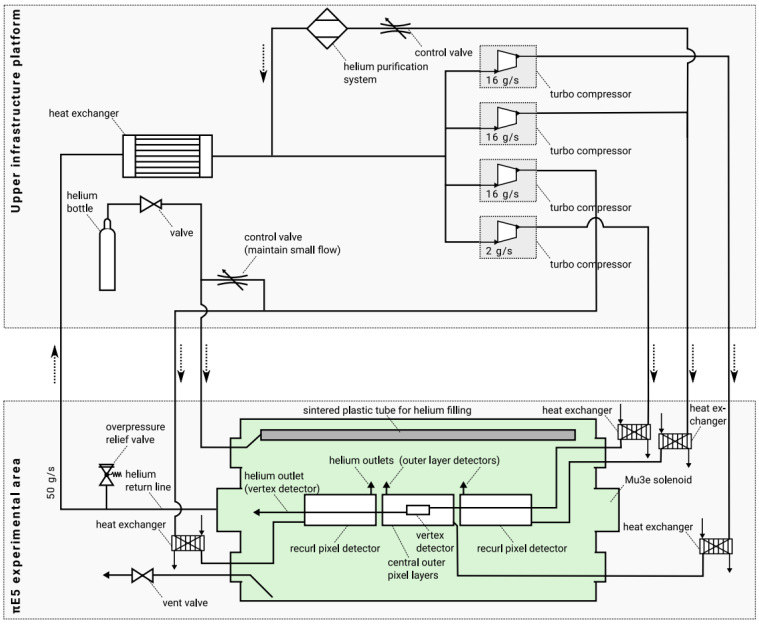

Figure 1.5: Flow diagram of the helium cooling infrastructure [22].

1.7 Ultralight silicon ladders

The MuPix sensors are mounted onto flexible multi-layered interconnection boards known as High Density Interconnect (HDI) circuits, which consist of thin aluminium traces deposited on flexible polyimide sheets. These circuits are responsible for transmitting both signal and power. To establish electrical connection, the sensors are bonded to the HDI using Single point Tape Automated Bonding (SpTAB), a technique that minimises the amount of bonding material and thereby keeps the material budget as low as possible. To read out the sensors, the HDI is also bonded at either end to interposer flex circuits, which transmit both signal and power to the end-piece flex printed circuit boards.

To enhance the mechanical stability, stiffeners are attached to the face of the sensors opposite to the HDI. These stiffeners were originally intended to incorporate cooling channels and to be constructed from two 25 µm thick polyimide films (Kapton®, DuPont), glued together to form a v-shape. However, recent design developments led to the adoption of carbon-fibre stiffeners. These are made of 25 µm thick unidirectional carbon fibre, co-cured with a 8 µm polyimide film layer and folded into a u-shape. A comparison between the polyimide film (v-fold) and carbon-fibre (u-fold) stiffeners is shown in Figure 1.6. The assembly of the sensors, HDI, interposer flex and mechanical support constitutes a self-supporting structure known as a ladder. In the following, ladders supported by polyimide film will be referred to as polyimide ladders, whereas ladders with a carbon-fibre support structure will be referred to as carbon-fibre ladders. Four ladders are combined into one module, except for Layer 2 modules, which are composed of five. The number of modules per layer, as well as the number of ladders and of MuPix sensors per ladder, varies depending on the detector layer. A complete breakdown of these quantities is provided in Table 1.1.

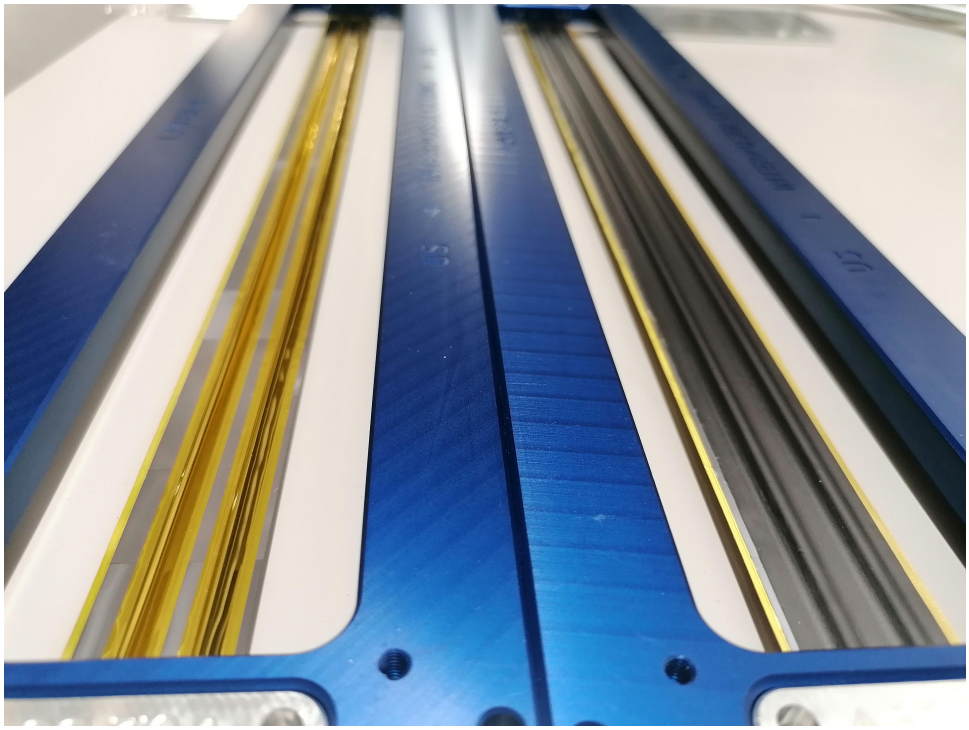

Figure 1.6: Image of a polyimide ladder (left) and a carbon-fibre ladder (right), each housed inside a blue aluminium ring frame.

Layer	**1**	**2**	**3**	**4**
Number of modules	2	2	6	7
Number of ladders	8	10	24	28
MuPix sensors per ladder	6	6	17	18
Ladder length	124.7 mm	124.7 mm	351.9 mm	372.6 mm
Minimum radius	23.3 mm	29.8 mm	73.9 mm	86.3 mm

Table 1.1: Pixel tracker geometry parameters of the central station, with the radius defined as the minimum distance of the MuPix sensors (excluding support structures) to the symmetry axis (beam line) [19].

1.8 Static misalignment and track-based alignment

The ladders are connected to the rest of the detector solely through the interposer flex circuits, as shown in Figure 1.7, which displays the complete end-piece region of a single module. This flexible mechanical connection allows for relative displacement of the MuPix chips with respect to the rest of the detector. In static conditions, such displacements can arise from gravitational sag or lifting effects due to different pressures above and below the ladder, for example, caused by the helium cooling flow. These static misalignments will be corrected using Track-Based Alignment (TBA) methods [23]. TBA is a software-based approach that reconstructs the precise positions of detector elements, by analysing known particle tracks [24].

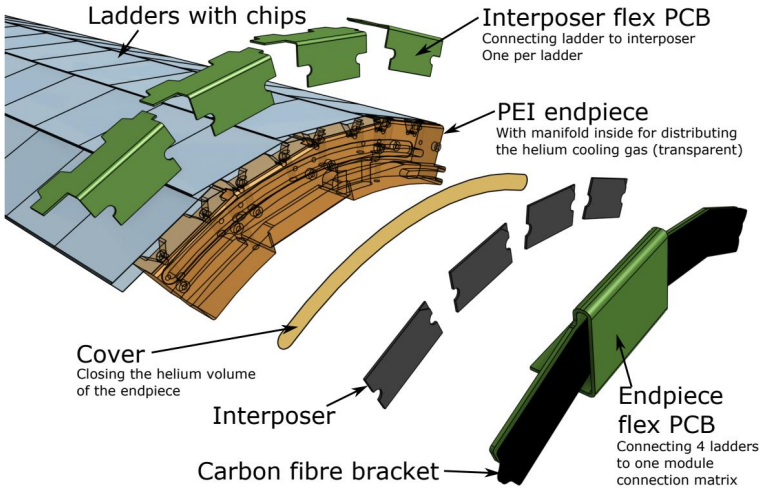

Figure 1.7: Outer layer assembly showing the end-piece region of a single module [19].

The effectiveness of TBA in the case of static misalignment of the Mu3e pixel detector is illustrated in Table 1.2, which shows the simulated improvement in signal reconstruction efficiency in the case of a misalignment corresponding to the expected sensor displacement after assembly.

Parameter	**Nominal**	**Misaligned**	**Aligned**
Efficiency (short)	100.0 %	5.9 %	99.7 %
Efficiency (long)	100.0 %	2.2 %	100.1 %
RMS $x_{\text{rec}} - x_{\text{true}}$	0.553 mm	0.724 mm	0.550 mm
RMS $y_{\text{rec}} - y_{\text{true}}$	0.555 mm	0.687 mm	0.552 mm
RMS $z_{\text{rec}} - z_{\text{true}}$	0.356 mm	0.813 mm	0.355 mm

Table 1.2: Signal reconstruction efficiency and vertex resolution for nominal, misaligned and aligned configurations of the pixel detector. The efficiencies are relative to the nominal configuration. The misaligned version corresponds to an estimate of the expected sensor misplacements after assembly [19].

1.9 Vibrations of outer pixel ladders

TBA techniques are highly effective in correcting static or slowly varying misalignments of detector components [25]. However, they are fundamentally limited in addressing high-frequency displacements, particularly those with periods shorter than the algorithm's runtime, which typically exceeds several seconds [23, 26]. Such dynamic misalignments, also called vibrations, remain uncorrected and can degrade the effective pixel resolution if large enough. While multiple scattering is the dominant contribution to track resolution in the low-energy regime of Mu3e, pixel resolution continues to play a crucial role in tasks such as track finding [27, 28, 29].

In the Mu3e detector, the primary sources of vibration originate from the helium-based cooling infrastructure. Two mechanisms are of particular concern: mechanical background motion transmitted by the helium compressors, dominated by a frequency peak at 100 Hz, and dynamic pressure fluctuations within the helium flow itself. Both can introduce time-dependent excitations of the detector ladders, potentially reducing resolution.

The aim of this thesis is to assess whether the mechanical stability of the Layer 4 ladders satisfies the stringent performance requirements of the Mu3e experiment. This is done by estimating an upper bound on the RMS vibrational displacement and evaluating whether the resulting pixel motion remains within acceptable limits or necessitates improvements to the mechanical design. The analysis is based on experimental measurements, simulation data, and vibrational modelling.

Chapter 2

The mechanics of vibration

This chapter outlines the theoretical framework that underpins the analysis presented in this work. The aim is not to provide a comprehensive overview, but rather to introduce the essential concepts and derive the relations required for the interpretation of the experimental data. Where appropriate, emphasis will be placed on the physical assumptions and approximations underlying each result, as these dictate the range of validity of the formulas employed.

2.1 Power spectral densities

Given a time dependent signal $x(t)$ with finite energy, i.e. a square integrable function $x(t) \in \mathbb{L}^2$, the energy spectral density (ESD) in the case of a symmetric convention is defined as the squared magnitude of its Fourier Transform (FT) [30]:

$$S_x(\omega) = |X(\omega)|^2, \tag{2.1}$$

where $X(\omega)$ denotes the FT of $x(t)$.

In situations where the integral of the squared signal does not converge, the above definition becomes ill-posed. In such cases, one considers the power spectral density (PSD), defined as:

$$S_x(\omega) = \lim_{T\to\infty} \frac{1}{T}|X_T(\omega)|^2, \tag{2.2}$$

where $X_T(\omega)$ is the Fourier transform of the truncated signal

$$x_T(t) = x(t) \cdot \Pi_T(t), \tag{2.3}$$

with $\Pi_T(t)$ denoting a rectangular window of width T. It is worth noting that care must be taken with the physical units associated with the PSD, as this is a frequent source of confusion. From dimensional analysis of the above definitions, it follows that the PSD carries units equal to the square of the signal's units divided by frequency. Specifically, for a signal with units $[x]$, the PSD has units

$$[S_x] = \frac{[x]^2}{\text{Hz}}. \tag{2.4}$$

For instance, if $x(t)$ denotes an acceleration signal with units m/s^2, then the corresponding PSD is expressed in m^2/s^3. In experimental contexts, particularly in vibration analysis, g^2/Hz, where g denotes the standard gravitational acceleration, is often used instead [31]. In contrast, the ESD carries the PSD units multiplied by time. In the remainder of this work, both the energy and power spectral densities will be referred to generically as the spectral density (SD).

2.1.1 Wiener-Khinchin theorem

At the core of many calculations in this work lies the Wiener-Khinchin theorem, which establishes that the SD and the autocorrelation function form a FT pair:

$$r_{xx}(\tau) = \frac{1}{\sqrt{2\pi}} \int_{-\infty}^{\infty} S_x(\omega)\, e^{\mathrm{i}\omega\tau}\, d\omega. \tag{2.5}$$

The autocorrelation function is defined as

$$r_{xx}(\tau) = \mathbb{E}\left[x(t)x^*(t-\tau)\right], \tag{2.6}$$

where $\mathbb{E}[\cdot]$ denotes the expectation operator and $x(t)^*$ is the complex conjugate of $x(t)$. Evaluating this expression at zero lag, $\tau = 0$, yields the second moment of the signal [32]:

$$r_{xx}(0) = \mathbb{E}\left[|x(t)|^2\right] = x_{\mathrm{RMS}}^2. \tag{2.7}$$

By the Wiener-Khinchin theorem, this quantity can equivalently be written in the frequency domain as

$$x_{\mathrm{RMS}} = \sqrt{\frac{1}{\sqrt{2\pi}} \int_{-\infty}^{\infty} S_x(\omega) d\omega}, \tag{2.8}$$

thus providing a direct link between the time domain variance and the integral of the SD, given a vanishing mean signal.

2.2 Physical models of the ladder

To analyse the vibrational response of the ladders, an appropriate physical model must first be established. In the most elementary approximation, the ladder is treated as a harmonic oscillator (HO), effectively modelled as a point mass while neglecting its spatial extent. This idealisation captures the essential dynamic behaviour but ignores deformation modes.

A more refined description models the ladder as a Bernoulli–Euler beam, thereby incorporating bending deformations in a single spatial direction while retaining the assumptions of small deflections and linear elasticity.

In the following subsections, both approaches are examined, and their respective linear response functions are derived. These results will form the basis for the quantitative analysis presented later in this work. The last subsection will extend the derivations to the coupled table-ladder system describing the shaker table.

2.2.1 Harmonic oscillator response function

A HO is a system whose dynamics are governed by a restoring force proportional to its displacement. Including damping and an external driving force, the equation of motion can be written as

$$m\frac{d^2x}{dt^2} + 2\gamma\frac{dx}{dt} + kx = F(t), \tag{2.9}$$

where m is the mass, γ the damping coefficient, k the spring constant, and $F(t)$ an external driving force.

We seek the linear response function $H(\omega)$, defined through the relation between the SD of the driving force $S_F(\omega)$ and that of the displacement $S_x(\omega)$:

$$S_x(\omega) = |H(\omega)|^2 S_F(\omega). \tag{2.10}$$

Applying the Fourier transform to the equation of motion yields

$$\big(- m\omega^2 + 2\mathrm{i}\gamma\omega + k\big)X(\omega) = F(\omega), \tag{2.11}$$

and hence

$$X(\omega) = \frac{F(\omega)}{k - m\omega^2 + 2\mathrm{i}\gamma\omega}. \tag{2.12}$$

Introducing the resonance frequency $\omega_0^2 = \frac{k}{m}$ and the quality factor $Q = \frac{m\omega_0}{2\gamma}$ we rewrite this as

$$X(\omega) = \frac{1}{k}\frac{F(\omega)}{1 - \frac{\omega^2}{\omega_0^2} + \mathrm{i}\frac{\omega}{Q\omega_0}}. \tag{2.13}$$

Taking the squared modulus gives

$$S_x(\omega) = \frac{1}{k^2}\frac{S_F(\omega)}{\big(1 - \frac{\omega^2}{\omega_0^2}\big)^2 + \big(\frac{\omega}{Q\omega_0}\big)^2}, \tag{2.14}$$

from which we derive the equation for the linear response function:

$$|H(\omega)| = \frac{1}{k}\frac{1}{\sqrt{\big(1 - \frac{\omega^2}{\omega_0^2}\big)^2 + \big(\frac{\omega}{Q\omega_0}\big)^2}}. \tag{2.15}$$

2.2.2 Bernoulli beam response function

We now move beyond the 1-dimensional approximation of the HO and model the ladder as a slender elastic beam. Although the beam exists in three spatial dimensions, we restrict the displacement to a single transverse direction, neglecting effects such as elongation, torsion, and bending in the orthogonal plane. As will become apparent when the motion is examined at a fixed point along the beam, the corresponding response function can be expressed as a sum over harmonic oscillator type modes with different weights. This framework naturally extends to more complex geometries, such as plate theory, while retaining a nearly universal linear response structure.

The transverse motion of the beam is governed by

$$\left(EI\frac{\partial^4}{\partial x^4} + c\frac{\partial}{\partial t} + \rho A\frac{\partial^2}{\partial t^2}\right) y(x,t) = F(x,t), \tag{2.16}$$

where $y(x,t)$ is the transverse displacement, EI is the flexural rigidity, c is a scalar uniform viscous damping constant, ρA is the mass per unit length, and $F(x,t)$ is the external driving force.

Since the force in our case depends on both time and space, a straightforward separation of variables is not applicable. Instead, we expand the displacement in terms of the spatial eigenfunctions (mode shapes) $\phi_n(x)$:

$$y(x,t) = \sum_n \phi_n(x) q_n(t), \tag{2.17}$$

where $q_n(t)$ are the time-dependent modal amplitudes.
Applying the Fourier transform in time to the full equation of motion yields

$$\sum_n \left(EI \frac{\partial^4 \phi_n(x)}{\partial x^4} - \rho A \omega^2 \phi_n(x) + \mathrm{i} c \omega \phi_n(x) \right) q_n(\omega) = f(\omega) g(x), \tag{2.18}$$

where we have assumed a separable forcing $F(x, \omega) = g(x) f(\omega)$.
Projecting both sides onto the basis functions $\phi_m(x)$ using the inner product, we obtain

$$\int \phi_m(x) \sum_n \left(EI \frac{\partial^4 \phi_n(x)}{\partial x^4} - \rho A \omega^2 \phi_n(x) + \mathrm{i} c \omega \phi_n(x) \right) q_n(\omega) dx = f(\omega) \int \phi_m(x) g(x) dx, \tag{2.19}$$

and using the eigenvalue relation

$$EI \frac{\partial^4 \phi_n(x)}{\partial x^4} = \lambda_n \phi_n(x), \tag{2.20}$$

together with the orthogonality of the eigenfunctions, we find

$$q_m(\omega) = f(\omega) \frac{\int \phi_m(x) g(x) dx}{\lambda_m - \rho A \omega^2 + \mathrm{i} \omega c}. \tag{2.21}$$

The general frequency-domain solution then reads

$$Y(x, \omega) = f(\omega) \sum_n \phi_n(x) \frac{\int \phi_n(x') g(x') dx'}{\lambda_n - \rho A \omega^2 + \mathrm{i} \omega c}. \tag{2.22}$$

For the specific case of symmetric forcing applied at both ends

$$g(x) = \frac{1}{2} \left[\delta(x - \frac{L}{2}) + \delta(x + \frac{L}{2}) \right], \tag{2.23}$$

this reduces to

$$Y(x, \omega) = f(\omega) \sum_n \phi_n(x) \cdot \frac{\phi_n\left(-\frac{L}{2}\right) + \phi_n\left(\frac{L}{2}\right)}{2\left(\lambda_n - \rho A \omega^2 + \mathrm{i} \omega c\right)}. \tag{2.24}$$

By introducing parameters ω_n and $\mathit{\Pi}_n$ in analogy with the harmonic oscillator, this expression can be rewritten as

$$Y(x, \omega) = f(\omega) \sum_n \frac{\phi_n^{'}(x)}{1 - \frac{\omega^2}{\omega_n^2} + \mathrm{i} \frac{\omega}{\mathit{\Pi}_n \omega_n}}, \tag{2.25}$$

where additional mode-dependent terms have been absorbed in $\phi_n(x)$, thus creating $\phi_n^{'}(x)$. When comparing this expression with Equation (2.13) it becomes evident that if the motion is examined at a fixed point $x = x_0$, the response reduces to a sum of harmonic oscillator terms, each associated with a normal mode and its own characteristic parameters.

2.2.3 Derivation of the table-ladder system response function

We now extend the description of Section 2.2.1 to include the coupling to the shaker table, as realised in the experimental setup. The essential difference lies in the fact

that the ladder is driven only through the spring damper connection to the table, rather than by a direct external force. As will become apparent, when the motion is examined in the frequency domain, the response function of the coupled system has the same form as that of an isolated harmonic oscillator with $H(0) = 1$, except for a multiplicative factor that remains close to unity in the parameter regime of interest.

Let $x(t)$ denote the displacement of the ladder in the laboratory frame, $x_b(t)$ the displacement of the table and

$$x_r(t) = x(t) - x_b(t), \tag{2.26}$$

their relative displacement. The spring exerts a force proportional to $x_r(t)$, while the damper exerts a force proportional to $\dot{x}_r(t)$, both acting on the ladder. This can be thought of as a car with a harmonic oscillator mounted on top, driving on a bumpy road; an illustration of this situation is shown in Figure 2.1. No additional direct forcing from the table motion is assumed.

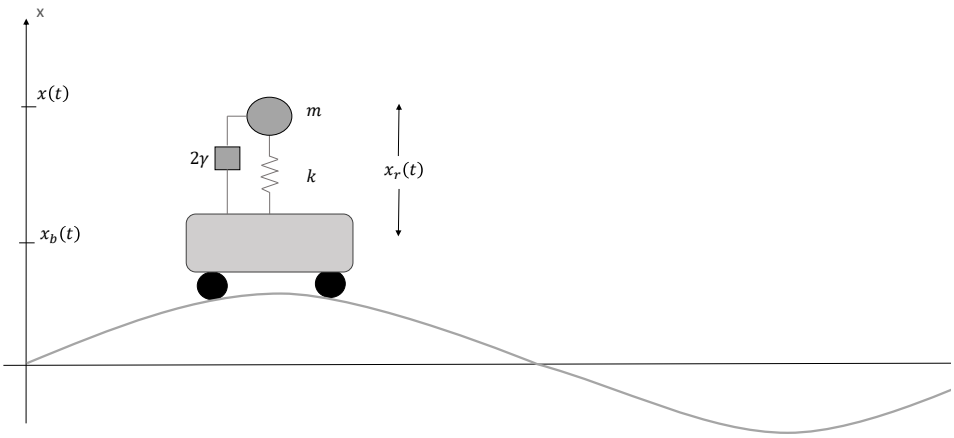

Figure 2.1: Analogy: a car with a HO mounted on top, driving over a bumpy road, representing a ladder placed on a shaker table excited with a sinusoidal signal.

The equations of motion are then

$$\ddot{x}_r(t) = \ddot{x}(t) - \ddot{x}_b(t) \tag{2.27}$$

$$\ddot{x}(t) = -\frac{\omega_0}{Q}\dot{x_r}(t) - \omega_0^2 x_r(t). \tag{2.28}$$

Applying the Fourier transform in time, with $\dot{X} \to i\omega X$, Eq. (2.28) becomes

$$-m\omega^2 X(\omega) = -2\mathrm{i}\omega\gamma\left[X(\omega) - X_b(\omega)\right] - k\left[X(\omega) - X_b(\omega)\right]. \tag{2.29}$$

Introducing the natural frequency $\omega_0^2 = \frac{k}{m}$ and the quality factor $Q = m\frac{\omega_0}{2\gamma}$, we obtain

$$X(\omega)\left[-\omega^2 + \omega_0^2 + \mathrm{i}\omega\frac{\omega_0}{Q}\right] = \left[\omega_0^2 + \mathrm{i}\omega\frac{\omega_0}{Q}\right] X_b(\omega). \tag{2.30}$$

Solving for $X(\omega)$ yields

$$X(\omega) = X_b(\omega) \cdot \frac{\omega_0^2 + \mathrm{i}\omega\frac{\omega_0}{Q}}{\omega_0^2 - \omega^2 + \mathrm{i}\omega\frac{\omega_0}{Q}}. \tag{2.31}$$

The magnitude of the numerator differs from ω_0^2 only by the slowly varying factor

$$\sqrt{\left(1 + \left(\frac{\omega}{Q\omega_0}\right)^2\right)}, \tag{2.32}$$

which is close to unity for the damping values and frequency values relevant here. Therefore, the coupled system behaves as

$$X(\omega) \approx X_b(\omega)\frac{1}{\sqrt{\left(1 - \frac{\omega^2}{\omega_0^2}\right)^2 + \left(\frac{\omega}{Q\omega_0}\right)^2}} = X_b(\omega) \cdot |H(\omega)|, \tag{2.33}$$

where $H(\omega)$ is the response function of a damped harmonic oscillator, normalised such that $H(0) = 1$. This shows that, in the regime of interest, the ladder displacement follows the table displacement through a transfer function nearly identical in form to that of an isolated harmonic oscillator, differing only by a constant prefactor. Note that this transfer function relates position SDs and is therefore dimensionless. We assume that an analogous relation holds for other models, such as the Bernoulli beam.

2.3 Fluid dynamics

When analysing results in Section 4.3.2, we compare the wind tunnel conditions at the University of Oxford with the helium-cooling environment of the experiment. For this comparison to be quantitative, we introduce a key dimensionless parameter from fluid dynamics, the Reynolds number, whose definition and physical significance will be discussed in the following subsection. We then outline a theoretical motivation for the expected scaling of the RMS displacement x_{RMS} with respect to both flow velocity and fluid density, providing a framework for interpreting the subsequent measurements.

2.3.1 Reynolds number

The Reynolds number Re quantifies the ratio of inertial to viscous forces acting on a fluid element [33]. It is a dimensionless parameter that serves as a primary indicator for distinguishing flow regimes around solid bodies [34]. Low values of Re typically correspond to laminar flow, whereas high values are associated with turbulence.

Formally, it is defined as

$$Re = \frac{\rho U_\infty L}{\mu}, \tag{2.34}$$

where ρ is the fluid density, U_∞ the free stream velocity (i.e. the velocity sufficiently far from any boundary layer), μ the dynamic viscosity of the fluid, and L the characteristic length scale. The definition of L depends on the geometry of the problem and standard conventions for the specific configuration under consideration.

For internal flows, such as those in pipes or ducts, it is common to take L as the hydraulic diameter,

$$D_h = \frac{4A}{P}, \tag{2.35}$$

where A is the cross-sectional area of the flow and P is the wetted perimeter.

When considering the boundary layer over a flat surface, the characteristic length becomes the distance from the leading edge $L = x$ and the corresponding Reynolds number is denoted:

$$Re_x = \frac{\rho U_\infty x}{\mu}. \tag{2.36}$$

2.3.2 Scaling behaviours of the RMS displacement

To estimate the RMS displacement, x_{RMS}, of an object with response function $H(f)$ placed in an air channel, we begin by considering the aerodynamic forcing. In reality, multiple aerodynamic force components contribute, but for a sufficiently large Reynolds number, the relevant terms exhibit the same velocity scaling, differing primarily by multiplicative coefficients [35]. We therefore combine them into a single effective term, writing the instantaneous force as

$$F_a(t) = \frac{1}{2}\rho v(t)^2 CA, \tag{2.37}$$

where ρ is the fluid density, A the effective exposed area, C a dimensionless coefficient, and $v(t)$ is the time-dependent flow velocity.

The corresponding SD of the force is

$$S_F(\omega) = \left(\frac{1}{2}\rho CA\right)^2 S_{v^2}(\omega), \tag{2.38}$$

where $S_{v^2}(\omega)$ is the SD of $v(t)^2$.

Applying the Wiener-Khinchin theorem, which has been introduced in Section 2.1.1, we obtain:

$$x_{RMS} = \sqrt{\frac{1}{\sqrt{2\pi}}\int_0^\infty S_F(\omega)|H(\omega)|^2 d\omega} = \frac{1}{2}\rho CA\sqrt{\frac{1}{\sqrt{2\pi}}\int_0^\infty S_{v^2}(\omega)|H(\omega)|^2 d\omega}, \tag{2.39}$$

where $S_F(\omega)$ and therefore also $S_{v^2}(\omega)$ are taken to be one-sided, thus changing the lower limit of integration to zero.

At this stage, the expression cannot be simplified further without assuming a particular form for $S_{v^2}(\omega)$. Assuming that neither $H(\omega)$ nor $S_{v^2}(\omega)$ depends explicitly on ρ, we find that

$$x_{\mathrm{RMS}} \propto \rho. \tag{2.40}$$

In the case of turbulent flow, under certain assumptions, we can get an estimate for the velocity scaling of x_{RMS}. Starting from the Wiener-Khinchin relation for the force:

$$\mathbb{E}[F(t)^2] = \int_0^\infty S_F(\omega, v, \rho) d\omega, \tag{2.41}$$

and substituting the aerodynamic force expression,

$$\mathbb{E}[F(t)^2] = \left(\frac{1}{2}\rho C A\right)^2 \mathbb{E}[v(t)^4]. \tag{2.42}$$

Decomposing $v(t) = \bar{v} + \delta v(t)$ into a mean component $\bar{v}$ and fluctuations $\delta v(t)$,

$$\mathbb{E}[v(t)^4] = \bar{v}^4 + 4\bar{v}^3 \cdot \mathbb{E}[\delta v(t)] + 6\bar{v}^2\sigma_v^2 + 4\bar{v} \cdot \mathbb{E}[\delta v(t)^3] + \mathbb{E}[\delta v(t)^4]. \tag{2.43}$$

For a statistically symmetric turbulent flow, odd central moments vanish, $\mathbb{E}\left[\delta v(t)^{2n+1}\right] = 0$ and velocity fluctuations scale linearly with $\bar{v}$ [36]. Thus,

$$\mathbb{E}[F(t)^2] \propto \rho^2\bar{v}^4. \tag{2.44}$$

If we assume that the relevant integrals in the displacement expression scale identically with velocity, then

$$x_{\mathrm{RMS}} \propto \rho\bar{v}^2. \tag{2.45}$$

The validity of this assumption is closely tied to the exact form of both functions and can change as variables, such as velocity, change. Nevertheless, we will see that, in a certain regime, this is a good approximation for the upcoming experiment.

Chapter 3

Background motion induced vibrations

In this chapter, the vibrational behaviour of carbon-fibre and polyimide ladders is investigated in the presence of background vibrations at the experimental site. Two experimental setups are introduced: the shaker table and the extendable ring frame. The shaker table was used to measure the vibrational response of the ladders to excitations with a fixed acceleration SD at selected frequencies. Measurements were performed at different positions along and across the ladders and compared to results from a modal analysis. The extendable ring frame was utilised to determine the dependence of the first mode frequency on the longitudinal tension applied to the ladder. From these measurements, the table–ladder system response functions were derived and, together with the background acceleration data, an estimate of the expected RMS displacement during operation was obtained using the Wiener-Khinchin theorem.

3.1 Shaker table

Shaker tables are mechanical platforms designed to produce controlled oscillatory motion. Structures placed on such a table experience vibrations corresponding to the selected excitation parameters, allowing for the systematic study of their dynamic response. Shaker tables are commonly used to investigate the vibrational behaviour of mechanical assemblies. Most commercially available systems operate at relatively high acceleration levels, often reaching several times the gravitational acceleration (g) [37]. While this is suitable for robust components, it poses a risk of damage to delicate objects such as silicon detectors. Moreover, high accelerations lead to large amplitudes, rendering some of the assumptions underlying the derivation of the response function less accurate. To mitigate this, the setup developed at the University of Oxford has been specifically designed to operate in the sub-milli-g regime, enabling the characterisation of fragile detector systems under non-destructive conditions.

The shaker table itself is constructed from carbon fibre, equipped with two piezoelectric actuators [38]. To reduce environmental interference, the entire setup is enclosed within a wooden box, which serves as an acoustic shield. Additionally, the system is placed on inelastic support platforms to minimise the influence of background vibrations present in the laboratory environment. The device under test (DUT), in this case a detector ladder mounted to a ring frame, is secured to the shaker

table using two clamps. The ring frame, a blue aluminium housing, is designed both to protect the ladders and to reproduce the experimental boundary conditions by clamping the interposer flexes. For displacement measurements, three capacitive sensors are employed. Two sensors monitor the motion of the shaker table, while the third records the vibrational response of the ladder at a chosen position. The sensors used are Micro Epsilon CS1 units in combination with the capaNCDT 6110 controller [39]. An overview of the setup is shown in Figure 3.1.

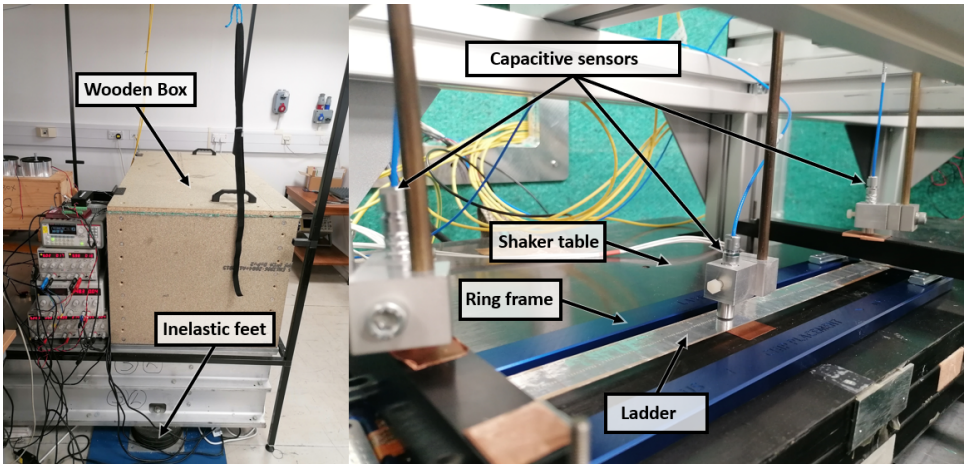

Figure 3.1: Photographs of the experimental setup: the wooden box resting on inelastic feet (left) and the open box showing the ladder inside the ring frame, mounted on the shaker table, along with three capacitive sensors (right).

The excitation of the shaker table is based on the inverse piezoelectric effect, where an applied voltage across a piezoelectric material induces microscopic strain, resulting in macroscopic displacement. In the present setup, a sinusoidal voltage signal is used to drive the system at a user-defined frequency. To ensure stable operation, accelerometers are employed in a feedback loop to continuously adjust the excitation amplitude, thereby maintaining the desired acceleration SD $S_a(f)$. Data acquisition is controlled via a custom LabVIEW interface [40], shown in the Appendix B.1. The interface allows for the adjustment of various experimental parameters, subject to two primary constraints:

First, according to the Nyquist–Shannon sampling theorem, the sampling frequency must be at least twice the highest excitation frequency to prevent aliasing [41]. Second, there exists a lower limit on the initial excitation frequency f_s, due to the finite input voltage that can be delivered to the piezoelectric actuator. At low frequencies, achieving the same acceleration requires proportionally larger displacements, since $a(f) = (2\pi f)^2 x(f)$. Because the displacement is proportional to the input voltage [42], and this voltage is limited, there is a minimum excitation frequency below which the system cannot reach the desired acceleration SD. This frequency threshold can be lowered by reducing the target acceleration SD. The relationship between two such configurations is given by:

$$\frac{f^1_{s,min}}{f^2_{s,min}} = \left(\frac{\mathrm{S}^2_{\mathrm{a}}}{\mathrm{S}^1_{\mathrm{a}}}\right)^{\frac{1}{4}}. \tag{3.1}$$

When the experiment is initiated, the software begins data acquisition at the initial excitation frequency f_s. The first few measurements are used to calibrate the capacitive sensors. This is achieved by assuming that, at frequencies sufficiently far from

the first mode frequency, the displacement of the shaker table and the test sample are identical. Under this assumption, the table monitoring sensors are calibrated to match the readings of the sample monitoring sensor.

Once the calibration is complete, the measurement sequence is restarted from f_s. For each frequency step, the system collects a predefined number of samples. The excitation frequency is then incremented and a short waiting period is inserted to allow the system to stabilise before proceeding to the next measurement. For each excitation frequency, the variance is obtained by fitting a sine curve at that frequency to the measured displacement data. Since the mean value of this vibrational movement vanishes, we denote this quantity RMS displacement in the rest of this work. The RMS value is then extracted using the relation $x_{\mathrm{RMS}} = \frac{A}{\sqrt{2}}$, where A denotes the amplitude of the fitted sine wave. The excitation frequency and the three resulting RMS values (two from the table sensors and one from the sample sensor) are recorded and saved for further analysis.

3.1.1 Extendable ring frame

During the first measurements, it became apparent that the vibrational behaviour of the ladder is strongly influenced by the precise boundary conditions. Extending the length of the ring frame caused the first mode frequency to nearly double for measurements of the same ladder. Since the expected RMS displacement during operation depends primarily on the position of the first mode frequency, as will be discussed in later sections, this behaviour warranted further investigation. To quantify the dependence of the ladder's response function on mechanical tension, a dedicated ring frame was designed and fabricated by the University of Oxford physics workshop. The key feature of this design was a movable base connected to the ladder via a load cell, enabling the controlled application of a measurable tensile force. A computer-aided design (CAD) rendering of the extendable ring frame is shown in Figure 3.2.

The implemented load cells were already operating near their maximum capacity at the default position. Owing to time constraints, neither the design nor the load cells could be modified. Consequently, an alternative approach was adopted: adjusting the distance in the extendable ring frame via the corresponding screw and measuring this distance directly instead of the applied tension.

3.2 Results

A series of ladder prototypes were evaluated using the shaker table. Various earlier designs, such as a carbon-fibre version with a 60 µm stiffener, as well as the current design, were tested at multiple positions on the ladder. The extendable ring frame was used exclusively to test the current 25 µm carbon-fibre ladder at its centre position. This section highlights the key results obtained for the current design, while additional measurements are provided in the appendix where relevant to the analysis and discussion.

3.2.1 Carbon-fibre and polyimide ladder measurements

The current design of the carbon-fibre ladder has been tested at its centre under a nearly constant acceleration SD of $10^{-5}\,\frac{\mathrm{m}^2}{\mathrm{s}^3}$ at the excitation frequency. For each excitation frequency, the system recorded data over a 1 s interval, resulting in a total of 2000 measurements per frequency step. Additional measurements with the same

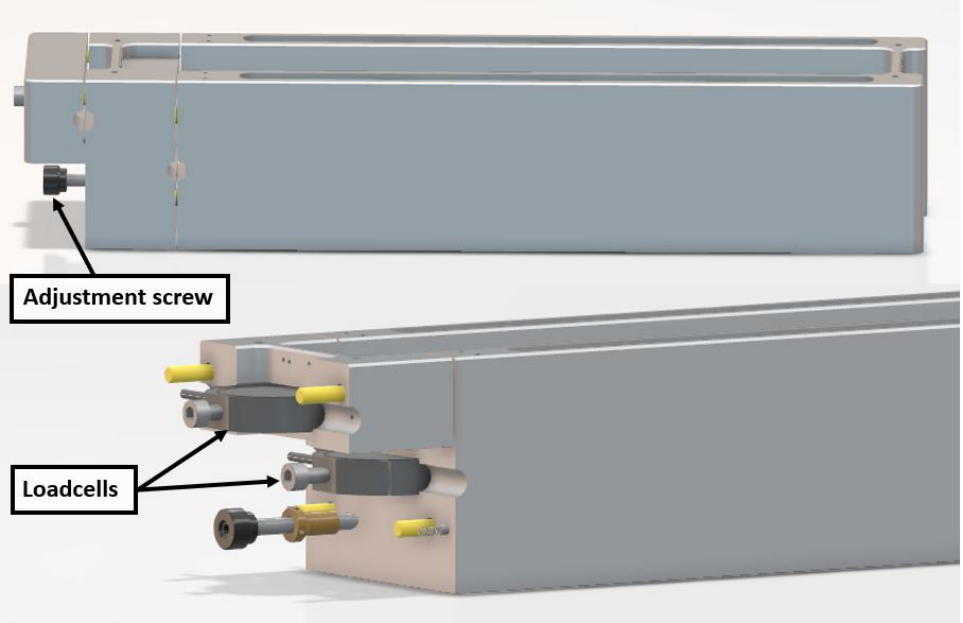

Figure 3.2: CAD drawing of the extendable ring frame. The upper image shows the complete assembly, while the lower image illustrates the structure with one part removed to reveal the installed load cells.

parameters have been conducted at different positions on the ladder to study its vibrational mode shapes. Equivalent measurements were carried out for the polyimide ladder, a lower acceleration SD of $10^{-6}\,\frac{\mathrm{m}^2}{\mathrm{s}^3}$ was applied. This reduced excitation amplitude allowed for a lower starting frequency and calibration frequency, thereby avoiding distortion of the sensor calibration by the first resonance peak. In order to compensate for the higher uncertainty, given the lower acceleration amplitude, 6000 measurements have been taken for each frequency step. All other measurement parameters were kept identical. The resulting vibrational responses of both ladders at their centre positions are shown in Figure 3.3. The black dots represent the calculated x_{RMS} of the accumulated measurement points for each excitation frequency, plotted along the x-axis. The shaded bands represent the combined measurement uncertainty of the capacitive sensor system on the RMS value, originating from sensor linearity, intrinsic resolution, and sensitivity deviation. The manufacturer's specifications were treated according to the Guide to the Expression of Uncertainty in Measurement (GUM), assuming a rectangular (equal-probability) distribution within the stated bounds [43]. As the measured displacement decreases with increasing frequency, the relative uncertainty increases accordingly, an effect visible in the higher frequency data. For sufficiently small RMS values, the associated measurement uncertainty exceeds the value itself, indicating that the result is not statistically distinguishable from zero. The uncertainty in the applied frequency is negligible across all frequency values.

In both cases, the displacement amplitude follows the expected inverse square frequency dependence, scaling as f^{-2}. The first vibrational modes were identified at $f_0 = 41.4\,\mathrm{Hz}$ for the carbon-fibre ladder and at $f_0 = 22.4\,\mathrm{Hz}$ for the polyimide ladder. A distinct feature is observed at approximately $f \approx 210\,\mathrm{Hz}$ in both measurements. As shown in Figure 3.4, a similar peak is present in the motion of the shaker table itself, suggesting that this feature might originate from resonances in coupled components of the setup rather than from the ladders themselves.

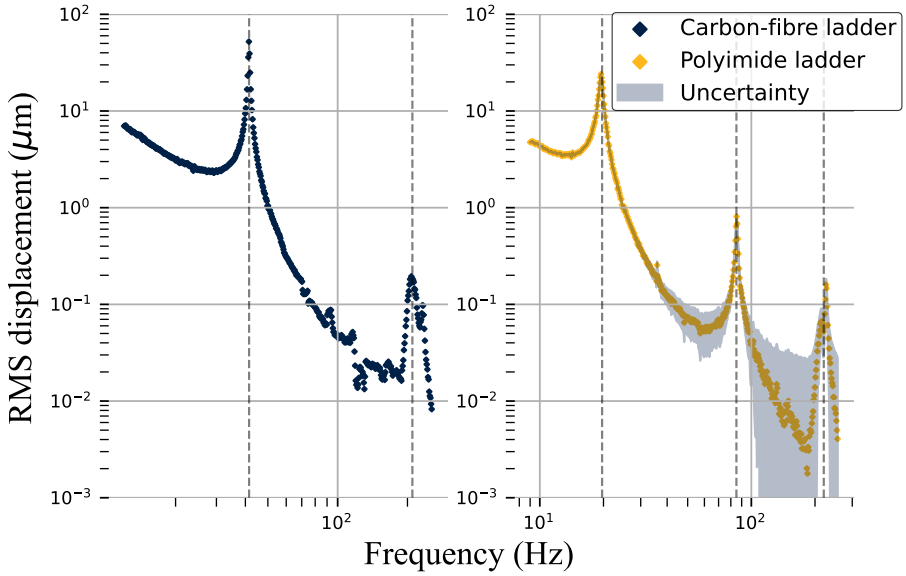

Figure 3.3: Measured RMS displacement as a function of excitation frequency at the centre of the carbon-fibre ladder (left) and the polyimide ladder (right). Shaded bands represent the uncertainties evaluated according to the GUM.

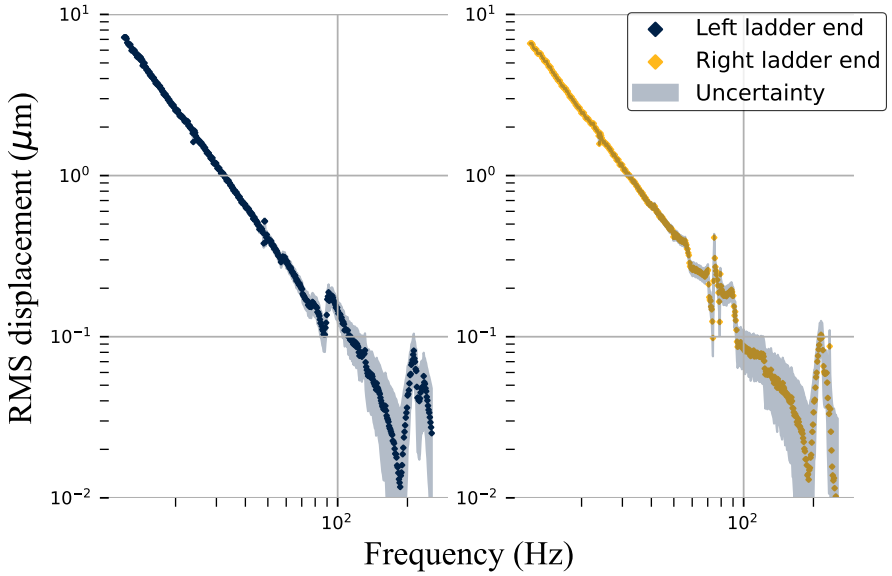

Figure 3.4: RMS displacement as a function of excitation frequency of the table at the left (left plot) and right (right plot) ends of the ladder. Shaded bands indicate uncertainties. In the analysis both results will be averaged.

Four measurements at increasing distances from the centre of the carbon-fibre ladder are shown in Figure 3.5. Each consecutive measurement was taken 3 cm further from the centre than the previous one. Comparing these results suggests the presence of a mode resembling the second mode of a string at $f_1 = 117.5\,\text{Hz}$, as indicated by the increasing amplitude up to a quarter of the ladder length followed by a decrease. In addition, an increasingly pronounced anti-peak appears between $f \approx 70\,\text{Hz}$ and $f \approx 80\,\text{Hz}$, which can be interpreted as an increase in phase lag as distance from the centre increases. Several other minor features are present; their origin is not obvious and may be related to the finite stiffness of the shaker table. Further investigation would be required to identify their nature. Since they are minor and therefore not expected to significantly affect the results, the investigation has not been carried out.

The same analysis was performed for the polyimide ladder. In this case, the second string mode is presumably located at $f_1 = 37.1\,\text{Hz}$, while a feature resembling the third mode of a simple string appears at $f_2 = 85.2\,\text{Hz}$. The corresponding plots are provided in the Appendix B.2.

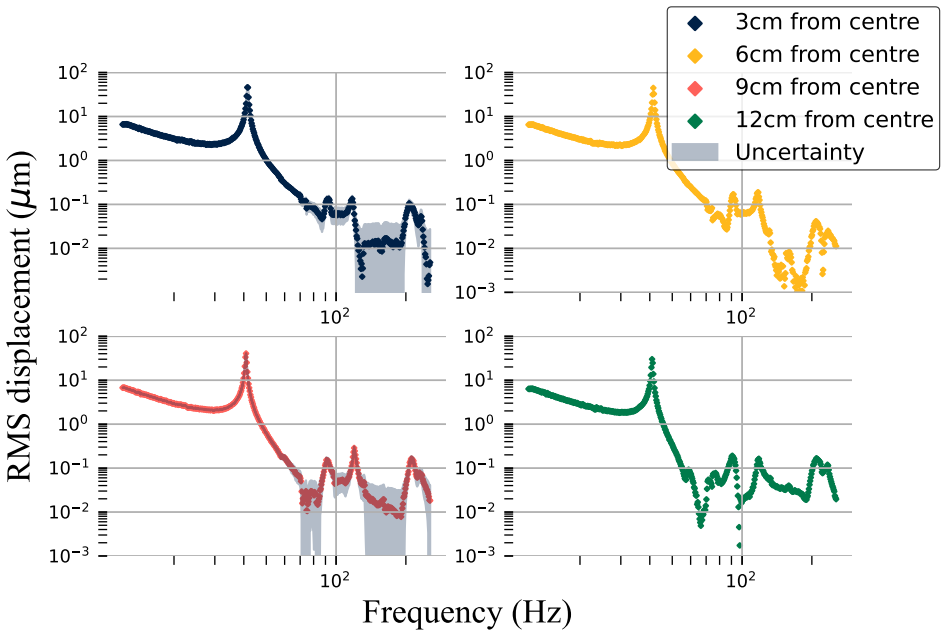

Figure 3.5: RMS displacement as a function of excitation frequency of the ladder at different locations along the ladder, starting at 3 cm from the centre. Each consecutive measurement is an additional 3 cm further away from the centre. Shaded bands indicate uncertainties.

3.2.2 Modal analysis

The modal analysis, based on finite element analysis (FEA), was carried out using the Mechanical Scenario Creation application within the 3DExperience software suite by Dassault Systèmes [44]. The CAD model of the carbon-fibre ladder used for the simulation is shown in Figure 3.6.

To avoid complications arising from material layers thinner than 10 µm, the composite structures were modelled using effective material approximations. Specifically, the Voigt (parallel loading) and Reuss (serial loading) models were applied

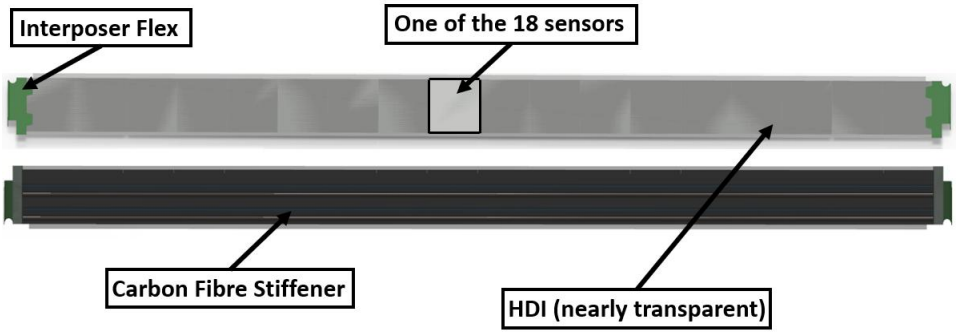

Figure 3.6: CAD model of the current carbon-fibre ladder design, shown from both the top and bottom view. The interposer flex, silicon pixel sensors, HDI, and carbon-fibre stiffener are labelled.

to derive homogenised material properties [45, 46]. The material composition ratios were obtained from internal Mu3e documentation, and the resulting property tables are provided in the Appendix A.1. Surface contacts between solids were modelled as epoxy layers with a thickness of 5 µm. The boundary conditions were defined as clamped at the interposer flexes, consistent with the experimental mounting scheme.

Due to time constraints, the simulation for the polyimide ladder employed the CAD geometry of the carbon-fibre ladder. As explained in Section 1.7, however, the stiffener geometries differ: the carbon-fibre stiffener has a hollow "u-fold" profile, whereas the polyimide film design uses two hollow "v-folds". Consequently, the carbon-fibre simulations are expected to agree more closely with the measurements than those of the polyimide ladder.

The modal analysis calculated the three lowest frequency eigenmodes. In the case of a carbon-fibre stiffener, the simulated fundamental mode was calculated to occur at $f_0 = 40.9\,\text{Hz}$ while for the polyimide film stiffener, the corresponding frequency is $f_0 = 28.1\,\text{Hz}$. A visualisation of the first vibrational mode of the carbon-fibre ladder is shown in Figure 3.7. The second eigenmodes were calculated to occur at $f_1 = 158.6\,\text{Hz}$ and $f_1 = 106.6\,\text{Hz}$ respectively, while the third modes came out to be at $f_2 = 341.5\,\text{Hz}$ for the carbon-fibre ladder and $f_2 = 226.3\,\text{Hz}$ for the polyimide ladder. As expected, the simulation results are in closer agreement with the experimental data for the carbon-fibre stiffener. A comparison between the results of the modal analysis and the shaker table measurements for both stiffener materials is shown in Table 3.1.

Materials	**Carbon fibre**		**Polyimide film**	
Source	Meas.	Sim.	Meas.	Sim.
1^{st} mode (Hz)	41.4	40.9	22.4	28.1
2^{nd} mode (Hz)	117.5	158.6	37.1	106.6
3^{rd} mode (Hz)	> 256	341.5	85.2	226.3

Table 3.1: Comparison of measured and simulated frequencies of the first three modes for the carbon-fibre and polyimide ladder.

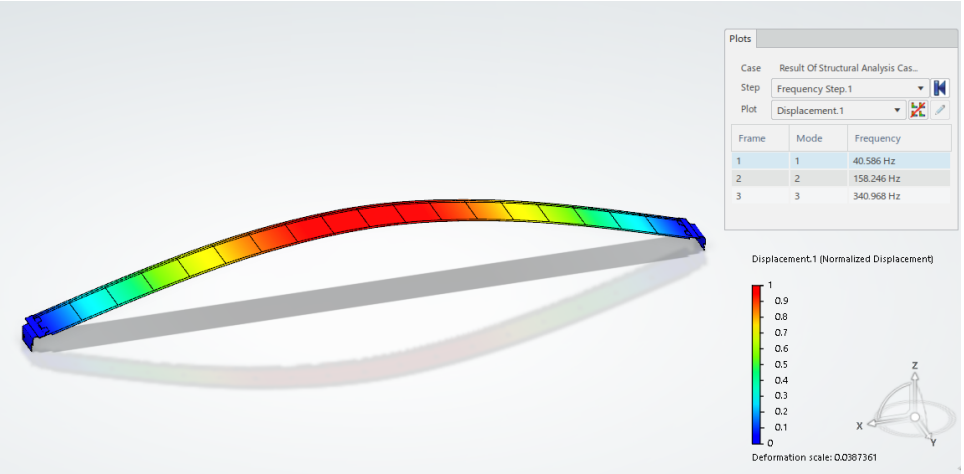

Figure 3.7: Simulated first mode of the current carbon-fibre design. The colour scaling indicates the relative displacement from the resting position. The frequencies corresponding to the first three modes can be seen in the "plots" window

3.2.3 Tension dependence of the first mode frequency

Using the extendable ring frame, the carbon-fibre ladder was measured for different elongations of the frame, corresponding to different applied tensions. Figure 3.8 shows the first mode frequency as a function of ring frame elongation. The ring frame initially had a gap of 1.5 ± 0.1 mm, which was taken as the reference. Consequently, the uncertainty in the first measurement is two-sided and smaller than in the subsequent measurements.

A square-root fit has been chosen as it reflects the expected behaviour of a string in a regime where Hooke's law is applicable. The error bars on the x-axis are too large to allow any definitive conclusion regarding the functional relationship between the two quantities. This is reflected in the reduced chi squared value of $\chi^2_\nu = 0.239$. During the measurements, the carbon-fibre stiffener began to peel off from the silicon sensors, as shown in Figure 3.9. This may explain the relatively low first mode frequency of 32.2 Hz observed in the relaxed position. The highest first mode frequency measured was 87.5 Hz, corresponding to a 172% increase relative to the relaxed position.

3.2.4 Mu3e background acceleration SD

The background acceleration SD was previously measured at PSI and the results obtained were kindly provided by the involved engineers. Nine accelerometers monitored all three spatial directions at three distinct locations around the magnet. A picture of the magnet with the highlighted sensor positions is shown in Figure 3.10. The acceleration measured at the magnet bracket was the highest. Therefore, we will proceed with that dataset for the upcoming analysis.

The acceleration SD was calculated using the Welch method [47]. This technique divides the time series data into segments of a chosen length, computes the Fast Fourier Transform (FFT) of each segment, and averages the resulting spectra. It also permits the specification of a window function (here a Hanning window) and an overlap value (here set to 66%). While this approach reduces the influence of noise on the spectral estimate, it does so at the expense of frequency resolution. With

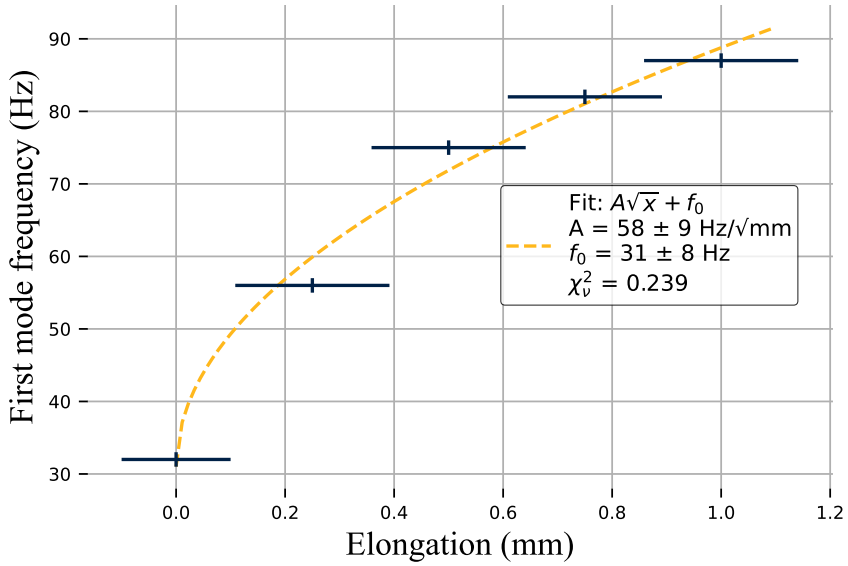

Figure 3.8: Measured first mode frequency as a function of ring frame elongation. The chosen fit function, parameters and reduced χ^2_ν are shown. The larger uncertainties, represented by error bars, stem from the distance measurement.

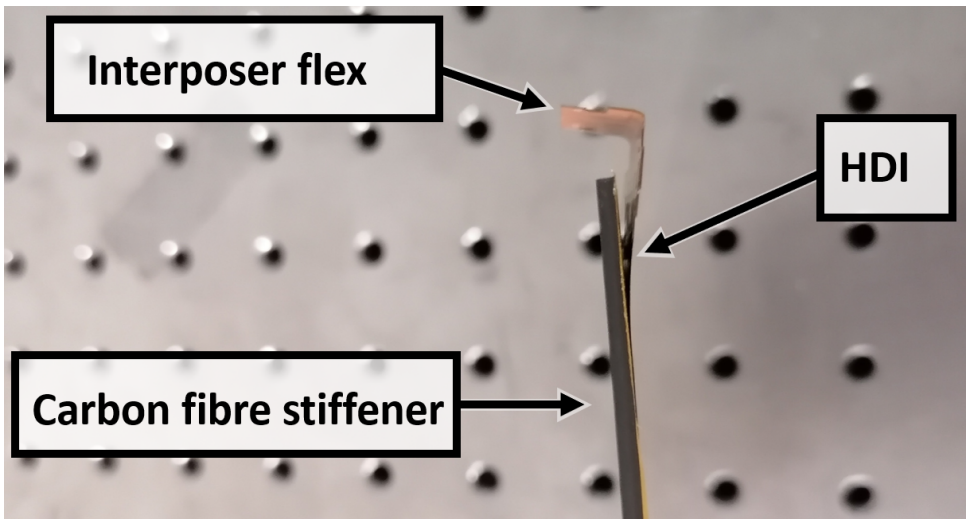

Figure 3.9: One end of a carbon-fibre ladder. The interposer flex having a copper colour and the black carbon-fibre stiffener are no longer attached.

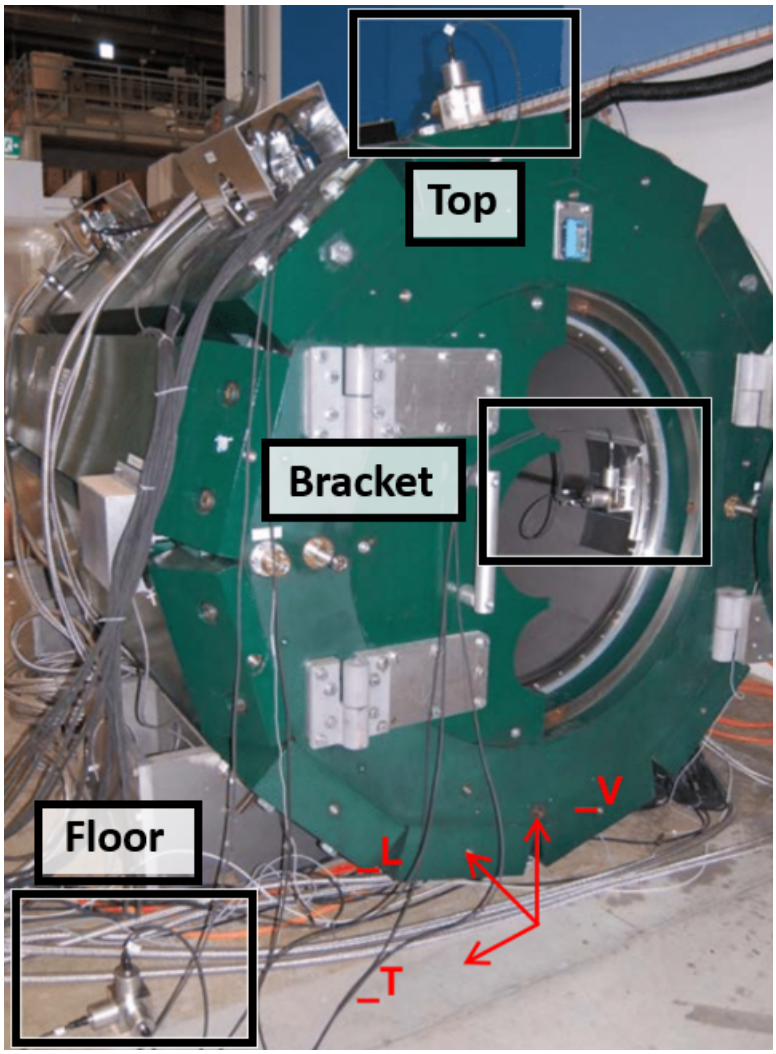

Figure 3.10: Photograph of the 1 T magnet used in the Mu3e experiment, equipped with three accelerometers mounted at distinct positions. Each accelerometer records motion along all three spatial directions. The red arrows indicate the transverse (T), longitudinal (L), and vertical (V) directions.

a sampling frequency of $f_s = 512\,\mathrm{Hz}$ and a segment length of $n = 1024$ samples, the frequency resolution is $\Delta f_{\mathrm{res}} = 0.5\,\mathrm{Hz}$. In addition to segmenting, other noise-reduction techniques were applied, including smoothing with a Savitzky–Golay (SG) filter [48] and the use of an envelope function. Figure 3.11 shows the calculated acceleration SD, in the transverse direction, as introduced in Figure 3.10, obtained using the Welch method combined with a third-order SG filter and the Welch method with an envelope fit.

3.3 Analysis

The analysis was carried out in two stages. First, the linear response function of the ladder was derived using the formulas and relations established in Chapter 2. This was then followed by predictions of the operational x_{RMS} values at various positions along the ladder, evaluated for different models and first mode frequencies.

3.3.1 Ladder response function

As explained in Section 2.2.3, the linear response function of the table–ladder system at the measured position is obtained by dividing the ladder displacement by the table displacement. In our case, the table movement is not perfectly uniform along its length. To account for this, we use the average displacement recorded by the two sensors monitoring the table as the base movement $X_b(f)$ in Equation (2.33). The fitted HO linear responses for the carbon-fibre and polyimide ladder at their centre position, $H(f)$, are shown in Figure 3.12. This fit only describes the first mode accurately. Higher order modes are not included in the 1D HO model and require a more sophisticated model, as introduced in Section 2.2.2. For cases involving multiple modes, the measured data can be fitted effectively using a fit with five distinct modes, hereafter referred to as the 5th-order fit, as demonstrated in Figure 3.13. The exact fit functions used can be seen in Table 3.2.

	HO fit	**5th-order fit**
Fit function	$\lvert H(f)\rvert = \dfrac{A}{\sqrt{\left(1-\frac{f^2}{f_0^2}\right)^2 + \left(\frac{f}{Qf_0}\right)^2}}$	$\lvert H(f)\rvert = \left\lvert \sum_{n=0}^{4} \dfrac{A_n}{1-\frac{f^2}{f_n^2} + \mathrm{i}\frac{f}{\Pi_n f_n}} \right\rvert$

Table 3.2: Comparison of fit functions: harmonic oscillator (HO) fit and 5th-order fit.

We expect the peaks of successive modes to decrease in amplitude at higher frequencies. This behaviour, however, cannot be reliably observed due to the increasing uncertainty at higher frequencies and the limited frequency range of the measurements. To improve interpretability, two approaches were employed to visualise the uncertainties determined using Gaussian error propagation. The first, also applied in the results section, adds or subtracts the estimated uncertainties from the calculated values, producing an error band. The second approach plots the uncertainties as a function of frequency, thereby emphasising their dependence on both frequency and the measurement value.

To better characterise the effect of higher order modes on the RMS displacement, a substantial portion of the carbon-fibre ladder was mapped through measurements at multiple distinct positions. A selection of these measurements is provided in the Appendix B.5.

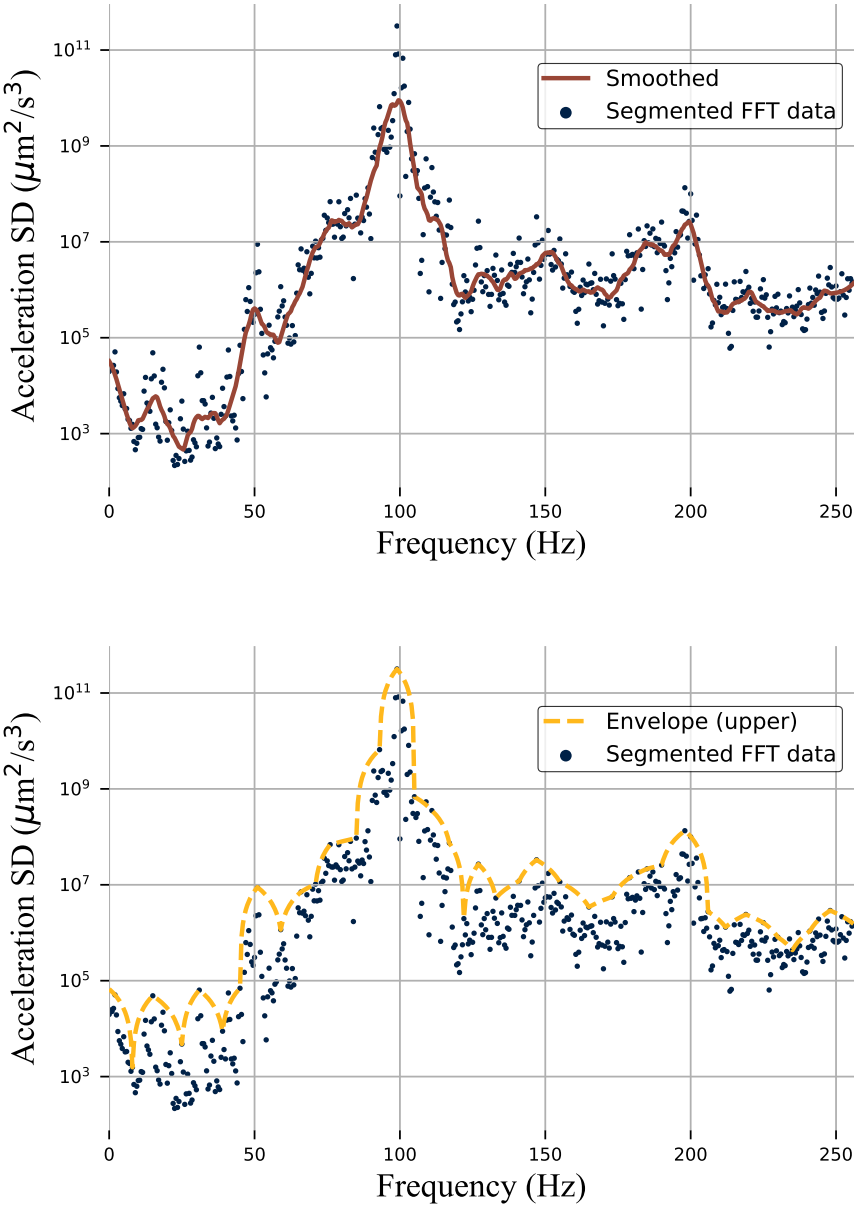

Figure 3.11: Plots of the acceleration SD in the transverse direction i.e. perpendicular to the beam direction, versus frequency. The upper plot is supplemented by a smoothed SG filter of order 3 whereas the lower plot includes an upper envelope fit to the data.

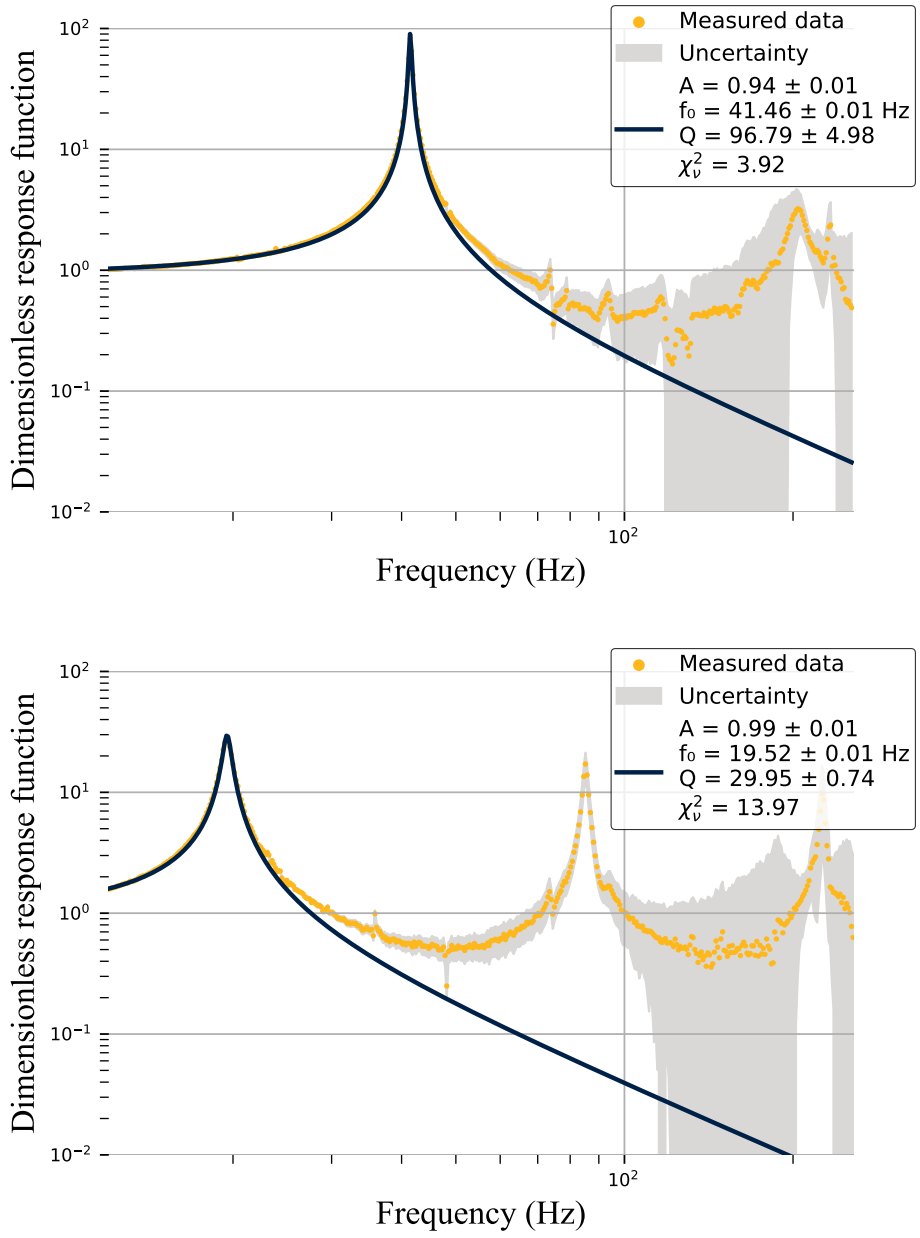

Figure 3.12: Linear response functions of the carbon-fibre ladder (top) and polyimide ladder (bottom) at the ladder centres. The entire displayed response function has been fit with the HO model given in Table 3.2. Fit parameters, their uncertainties and the reduced χ^2_ν value are displayed in the legend. Both values are much larger than 1 reflecting the use of a model of limited validity.

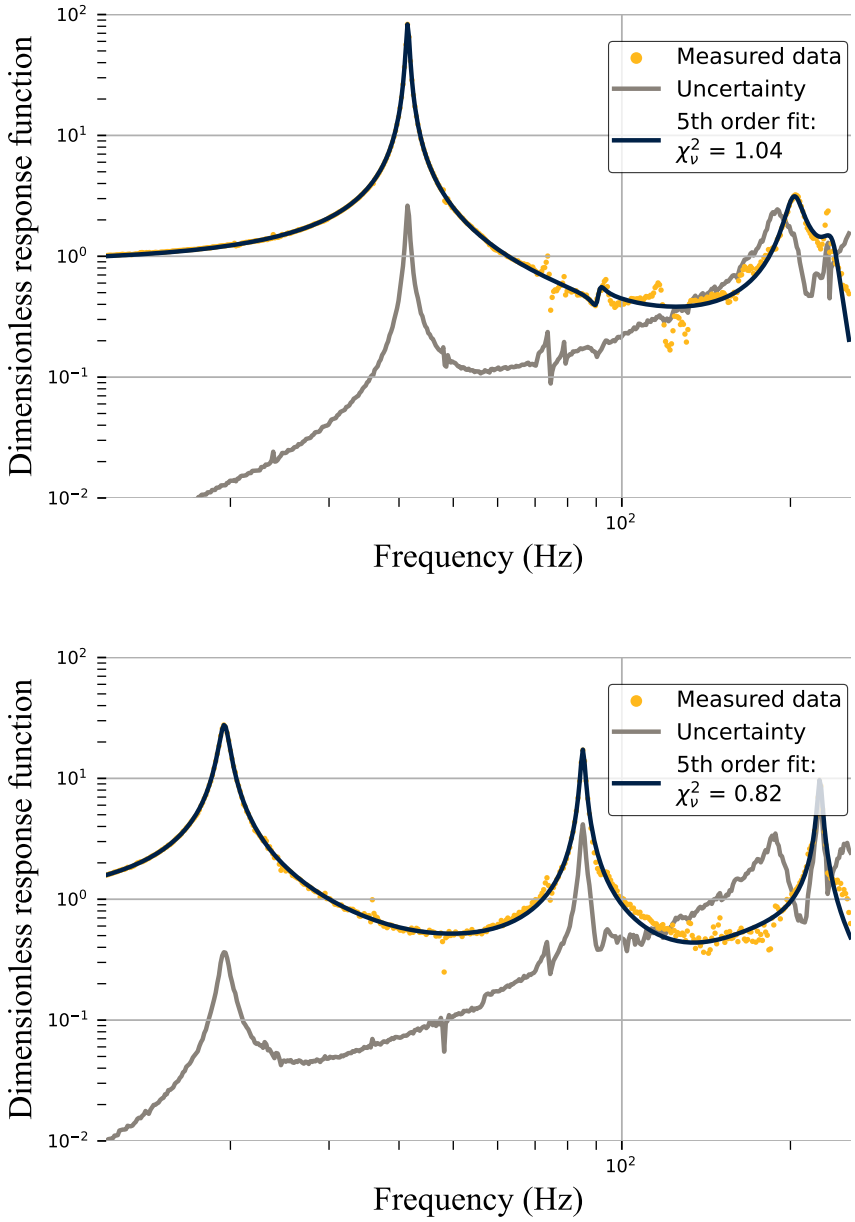

Figure 3.13: Linear response functions of the carbon-fibre ladder (top) and polyimide ladder (bottom) at the ladder centres. The response function has been fit with a 5th-order model given in Table 3.2. The reduced χ^2_ν values are displayed in the legend, both values are close to 1 indicating a good agreement between model and data. The uncertainties are shown explicitly as a function of frequency, rather than as shaded bands as in previous figures.

3.3.2 Expected displacement due to background vibration

By combining the acceleration SD measurements with the response function derived from the shaker table experiment, the RMS displacement during operation can be predicted using the Wiener-Khinchin theorem:

$$x_{\mathrm{RMS}} = \sqrt{\int S_x(f)|H(f)|^2 df} = \sqrt{\int \frac{S_a(f)}{(2\pi f)^4}|H(f)|^2 df}. \tag{3.2}$$

For the current carbon-fibre ladder, x_{RMS} has been evaluated using the HO model and a 5th-order model. Measurements were taken at 15 distinct points distributed along the length and width of the ladder, all on one side. Exploiting the symmetry of the ladder with respect to the mid-plane parallel to its shorter axis, the results were mirrored. The resulting contour plots are shown in Figure 3.14 (HO model) and Figure 3.15 (5th-order model). The results incorporate the acceleration SD of all three spatial directions. The segmented SD data were used directly, without applying either an envelope fit or a SG filter. For the HO model, the maximum displacement occurs at the centre of the ladder under transverse excitation, reaching 1.5 µm. In the case of the 5th-order model, the maximum value is found to be 2.4 µm at the edge of the ladder, owing to the higher value of the response function near 100 Hz at that position. No uncertainties can be provided given the lack of information about the errors on the acceleration SD.

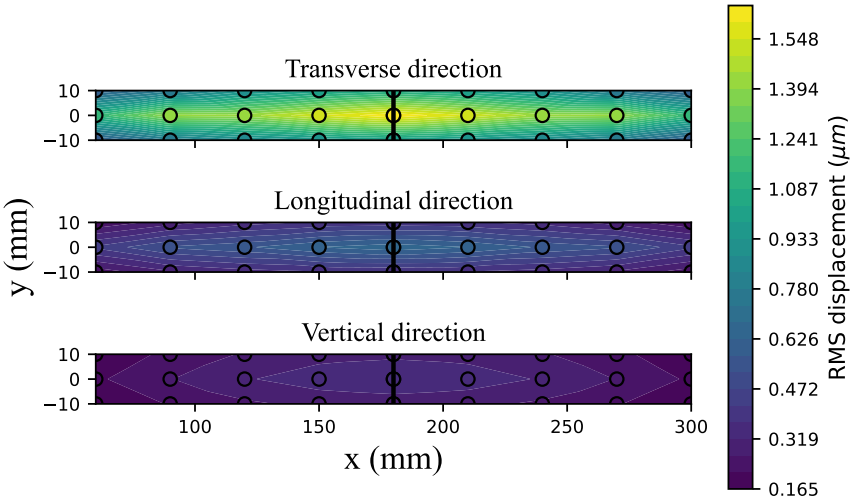

Figure 3.14: RMS displacement predicted by a HO model for multiple points on a section of the carbon-fibre ladder. Measured positions are shown as black circles; intermediate values were determined by linear interpolation. The central black line indicates the plane of symmetry used for mirroring the results.

For the HO model, the polyimide ladder exhibits smaller overall displacement values, primarily because its first mode is farther from 100 Hz. The highest displacement predicted for the polyimide ladder is approximately 1.2 µm. In the case of the 5th-order model, the behaviour changes and the polyimide ladder exhibits more

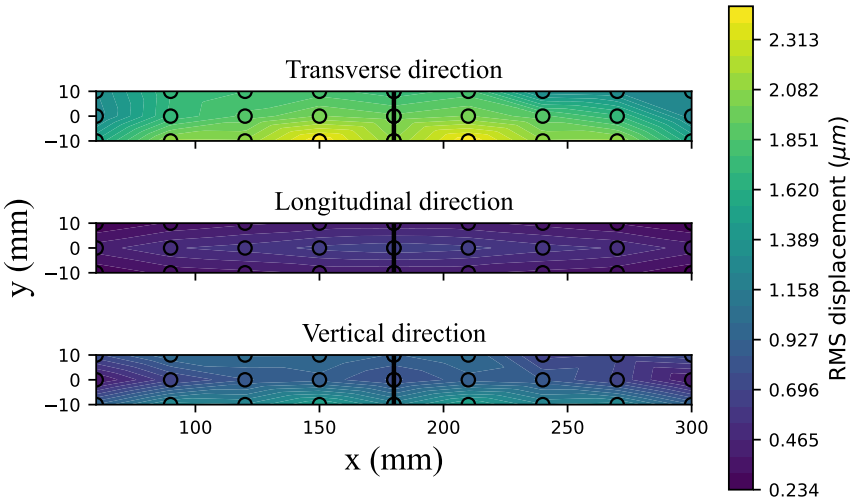

Figure 3.15: RMS displacement of a 5th-order model for multiple points on a section of the carbon-fibre ladder. Measured positions are shown as black circles; intermediate values were determined by linear interpolation. The central black line indicates the plane of symmetry used for mirroring the results.

vibrational movement at the centre, reaching 2.2 µm. This shift occurs due to the spectral feature in the polyimide ladder response located near 100 Hz.

Assuming that the quality factor remains constant as the tension increases, the ladder movement can be estimated for different first mode frequencies using a HO model. The resulting RMS displacement as a function of first mode frequency, obtained using three distinct methods of analysing the acceleration SD, is shown in Figure 3.16. As expected, the envelope fit, which corresponds to interpolated curves between maximum values, yields the largest results, while the SG filter reduces the integrals in nearly all cases. For the specific case of a first mode at 100 Hz, the contour plot of the ladder displacement, constructed directly from the segmented data without SG filtering or envelope fitting, is presented in Figure B.8. In this case, the predicted maximum displacement exceeds 90 µm.

3.4 Discussion

The shaker table proved reliable in predicting the first mode frequency but was less effective at capturing higher frequency modes due to the rapid increase in uncertainty with frequency. This limitation could be mitigated by employing more precise measurement techniques, such as a laser Frequency Scanning Interferometry (FSI) system. However, depending on the acceleration SD, this may be unnecessary, as higher frequency contributions are suppressed in the integral expression from Section 2.1.1 by a factor of $(2\pi f)^{-4}$. From Figure 3.16, it can be deduced that modes above 150 Hz do not contribute significantly to the integral.

The modal analysis predicted the first mode of the carbon-fibre ladder with a relative difference of 1.2%. For the polyimide ladder, the relative difference was larger than

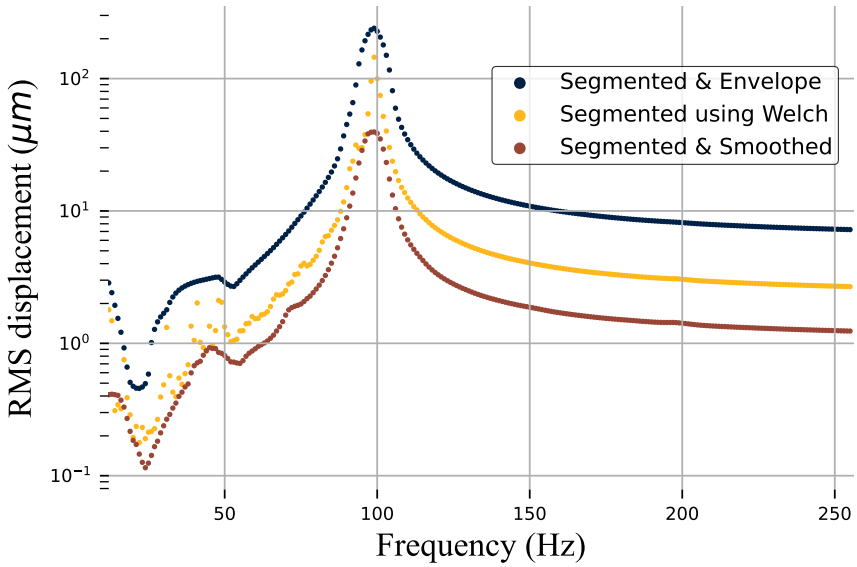

Figure 3.16: Expected displacement of the centre of the carbon-fibre ladder as a function of the first mode frequency, evaluated using the HO model. The analysis is based on the transverse acceleration SD (perpendicular to the beam). Three methods of analysing the data are shown, all segmented using the Welch method: the envelope function yields the highest values, while smoothing tends to give the lowest.

20%. The better agreement for the carbon-fibre ladder can be attributed to the use of its actual CAD model in the simulation. In contrast, the polyimide stiffener has a different geometry, using less material overall, which results in a lower measured value. Higher order modes were not reproduced reliably, likely due to mesh quality limitations. Thin features, particularly the curved and slender stiffener, require a large number of mesh elements and substantial computational resources to be modelled accurately. Additional discrepancies may arise from internal symmetries preserved in the CAD model but broken in the physical ladder, or deviations in the effective properties of the composite materials from those predicted by conventional homogenisation rules such as the Reuss or Voigt models.

The design of the mechanical support for the ladders has been a topic of extensive ongoing discussion. One proposal to increase ladder stiffness was to extend the stiffener and connect it to the end pieces. The modal analysis predicts a first mode resonance frequency of $f_0 = 83\,\text{Hz}$ for this configuration. Similar frequencies can also be achieved by increasing the applied tension, as shown in Figure 3.8, which has the advantage of keeping the material budget unchanged. Increasing the stiffener thickness also raised the first mode frequency, but only to $f_0 = 48.7\,\text{Hz}$ as depicted in Figure B.4. However, a proper comparison necessitates precise tension quantification. If additional stability is required in the future, modifying the boundary conditions appears to be the most effective strategy. In all cases, the first mode frequency should be measured to ensure it remains sufficiently far from the acceleration SD peak.

In summary, the most critical aspect in designing a mechanical structure is to account for resonance frequencies and potential coupling to other components. In the case of the Mu3e experiment, ladder vibrations are negligible compared to the pixel resolution as long as the first mode frequency does not lie near 100 Hz. At this frequency, depending on the averaging method used for the acceleration SD, displacements are predicted to reach nearly 100 µm, approximately four times the pixel resolution. However, for the experimentally determined first mode frequencies in this work, even when using an envelope fit, the expected displacement remains below 3 µm.

Chapter 4

Cooling flow induced vibrations

In this chapter, the vibrational behaviour of the carbon-fibre and polyimide ladder in an airflow is investigated to estimate their RMS displacement during operation in a cooling flow. For this purpose, a wind tunnel was assembled at the University of Oxford. Two approaches are combined: experimental measurements in the wind tunnel and CFD simulations. The CFD simulation of the wind tunnel is compared to a simulation of the cooling flow deployed in the experiment, allowing the measured values to be placed into context. Finally, the two setups themselves are compared using their Reynolds numbers.

4.1 Wind tunnel

The excitation spectrum induced by a gaseous cooling flow is too complex to be reproduced with a simple shaker table. To specifically study the vibrational response of the ladder to such cooling flow induced vibrations, a dedicated wind tunnel setup has been assembled.

The wind tunnel consists of a series of white PVC tubes connected to an industrial fan. The fan expels air from the tube system, creating a pressure gradient that induces a continuous airflow. The setup includes a specially designed tube and separate clamps to hold the ladder in place, as illustrated in Figure 4.1. The interior geometry of the holder was tailored to approximate the boundary conditions of the actual Mu3e detector. To reduce flow turbulence and improve measurement reproducibility, the test section was positioned immediately downstream of a long, straight segment of tubing. This configuration promotes a stable and uniform flow profile. The custom tube includes a sensor inlet on its top side, enabling the placement of a capacitive displacement sensor for vibration measurements. Because the sensor must be located in close proximity to the DUT, perturbations of the local flow behaviour are expected. However, simulations indicate a smaller airflow velocity on the ladder side where the sensor is mounted; thus, any such effects are expected to be small and are therefore neglected. The airflow was monitored using a hot-wire anemometer, the Testo 405i model [49], at both upstream and downstream positions. Near the end of the downstream section, close to the fan, a simple adjustable valve was integrated into the tubing. This valve allows control of the internal pressure and thereby modulates the flow velocity, compensating for the limited adjustability of the fan's power output.

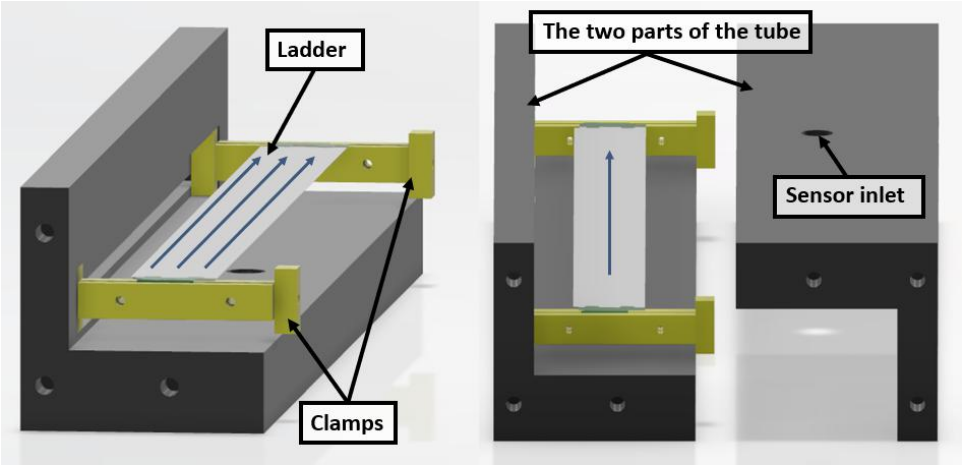

Figure 4.1: CAD model of the custom-made tube, showing one half of the assembly (left) and both halves separated, which are ultimately screwed together to complete the tube (right). Yellow 3D-printed clamps are used to fix the ladder and reproduce the experimental boundary conditions, blue arrows denote the direction of airflow along the ladder.

An overview of the partial wind tunnel setup CAD model, without the fan and valve, is shown in Figure 4.2, while the assembled experimental setup is shown in Figure 4.3.

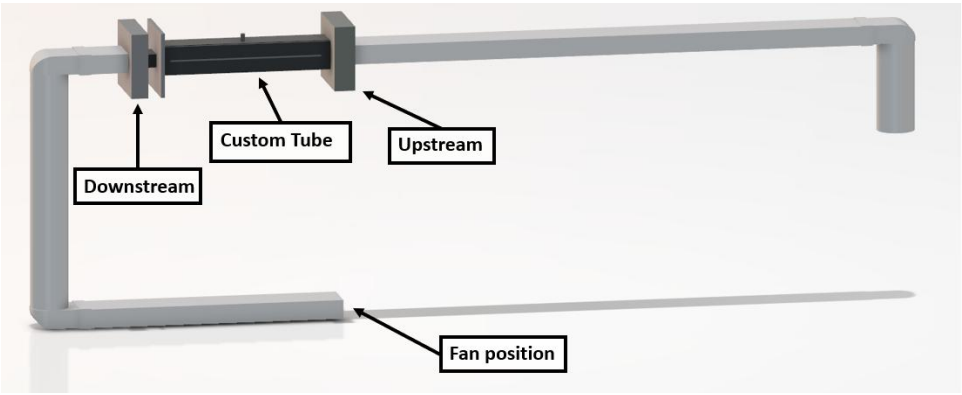

Figure 4.2: CAD of the airflow setup used in the CFD simulation. The fan connects to the square tube at the bottom, pulling air through the system. The custom tube is inserted between the greyish aluminium squares and has a little black cylinder on top, representing the capacitive sensor.

The data acquisition process for the wind tunnel setup is simpler than that for the shaker table. It is managed using a custom Python script that allows the user to specify both the acquisition rate and the total measurement duration. The recorded voltages, together with their corresponding timestamps, are saved for subsequent analysis.

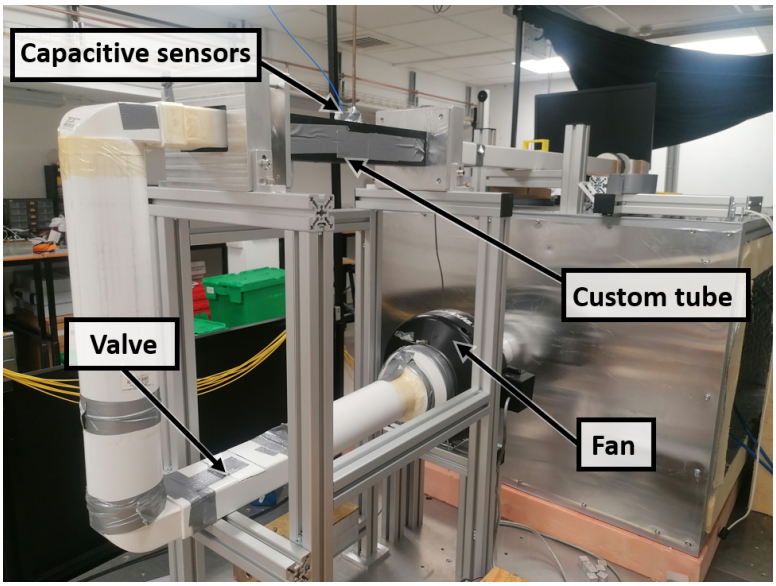

Figure 4.3: Photograph of the airflow setup used at the University of Oxford. The blue cable connects to the capacitive sensor inside the custom tube. The black industrial fan is visible at the lower centre, with the custom valve shown in its closed position.

4.2 Results

Cooling induced vibrations were studied for both the carbon-fibre and polyimide ladder. In addition, a CFD simulation of the setup was performed to enable comparison with simulations of the Mu3e cooling system. Both sets of results are presented in this section.

4.2.1 Velocity dependence of vibrations

The x_{RMS} of airflow-induced vibrations was measured for both the carbon-fibre and polyimide ladder at their midpoints. Upstream and downstream velocities were monitored for 50 s before removing the hot-wire anemometer and initiating the displacement measurement. Displacement data were acquired at 512 samples per second for 60 s. The displacement and airflow measurements were not performed simultaneously in order to maintain a homogeneous upstream flow; previous tests showed that placing the hot-wire anemometer in the airflow altered the ladder's vibrational response, distorting the results.

Systematic differences between upstream and downstream velocities were observed, with upstream values consistently higher for the same fan setting. Their relationship is shown in Figure 4.4, where a linear fit was applied. The hot-wire anemometer uncertainties have been determined from the accuracy listed by the manufacturer, being $0.1\,\mathrm{m\,s^{-1}} \pm 5\%$ m.v. below $2\,\mathrm{m\,s^{-1}}$ and $0.3\,\mathrm{m\,s^{-1}} \pm 5\%$ m.v. above, assuming again an equal probability distribution.

A more homogeneous flow was measured upstream of the ladder; therefore, the upstream velocities were used for subsequent measurements and analysis. The dependence of the RMS displacement at the ladder centre on the averaged upstream velocity is shown in Figure 4.5 for both the polyimide and carbon-fibre ladder. The pixel resolution of 23 µm is indicated by the dotted line. Although this quan-

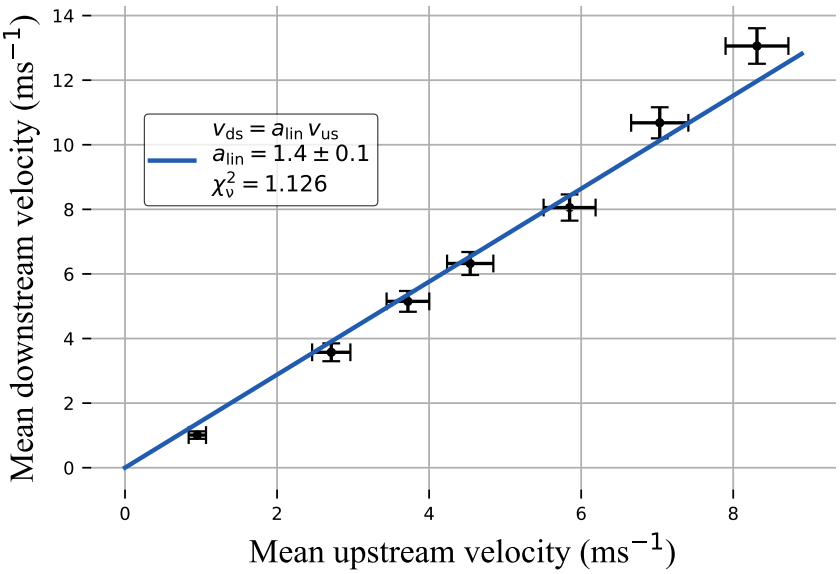

Figure 4.4: Downstream velocity v_{ds} as a function of the upstream velocity v_{us}. The fit function, fit parameter with uncertainty, and reduced χ^2_ν are shown in the legend, while error bars indicate the uncertainties on the measured values.

tity represents an in-plane resolution and not an out-of-plane displacement such as x_{RMS}, we include it as a reference since it is commonly used in comparisons with multiple scattering. In both cases, a quadratic fit was applied for velocities below $5.3\,\mathrm{m\,s^{-1}}$. Above this threshold, a sudden change in slope was observed, after which a linear fit was used. In all cases, the reduced $\chi^2_\nu \ll 1$, indicating that the measurement uncertainties are likely overestimated and that various fitting approaches could describe the behaviour effectively. The carbon-fibre ladder exhibited a lower first mode frequency than expected, likely due to the stiffener peeling off from the silicon sensors, as shown in Figure 3.9. For the polyimide ladder, the tension was increased, shifting the first mode to 34 Hz. This adjustment was necessary because, at lower tension, the vibrational amplitude of the polyimide ladder exceeded 150 µm at high velocities, surpassing the measurement range of the capacitive sensor. When mounting the ladder in the custom tube, the polyimide stiffener started detaching from the silicon sensors in a similar way to the carbon-fibre ladder.

For the polyimide ladder, the RMS displacement reached $82.2 \pm 0.6\,\mu\mathrm{m}$ at an average upstream velocity of $8.5 \pm 0.4\,\mathrm{m\,s^{-1}}$. The carbon-fibre ladder displayed less motion overall, with a maximum x_{RMS} of $57.9 \pm 0.6\,\mu\mathrm{m}$ at $8.3 \pm 0.4\,\mathrm{m\,s^{-1}}$. The low sampling frequency of the hot-wire anemometer ($f_{sample} = 1\,\mathrm{Hz}$) prevents the airflow's spectral data from yielding useful information.

4.2.2 Computational fluid dynamics simulation

The CFD simulation was performed using Autodesk CFD 2026 [50]. A static simulation of the setup shown in Figure 4.2 was carried out, modelling air as a compressible fluid. A boundary condition and an initial condition representing the fan action were applied. The results of the CFD simulation with a fan flow velocity of $4\,\mathrm{m\,s^{-1}}$ are shown in Figure 4.6. The simulated upstream velocity at the mea-

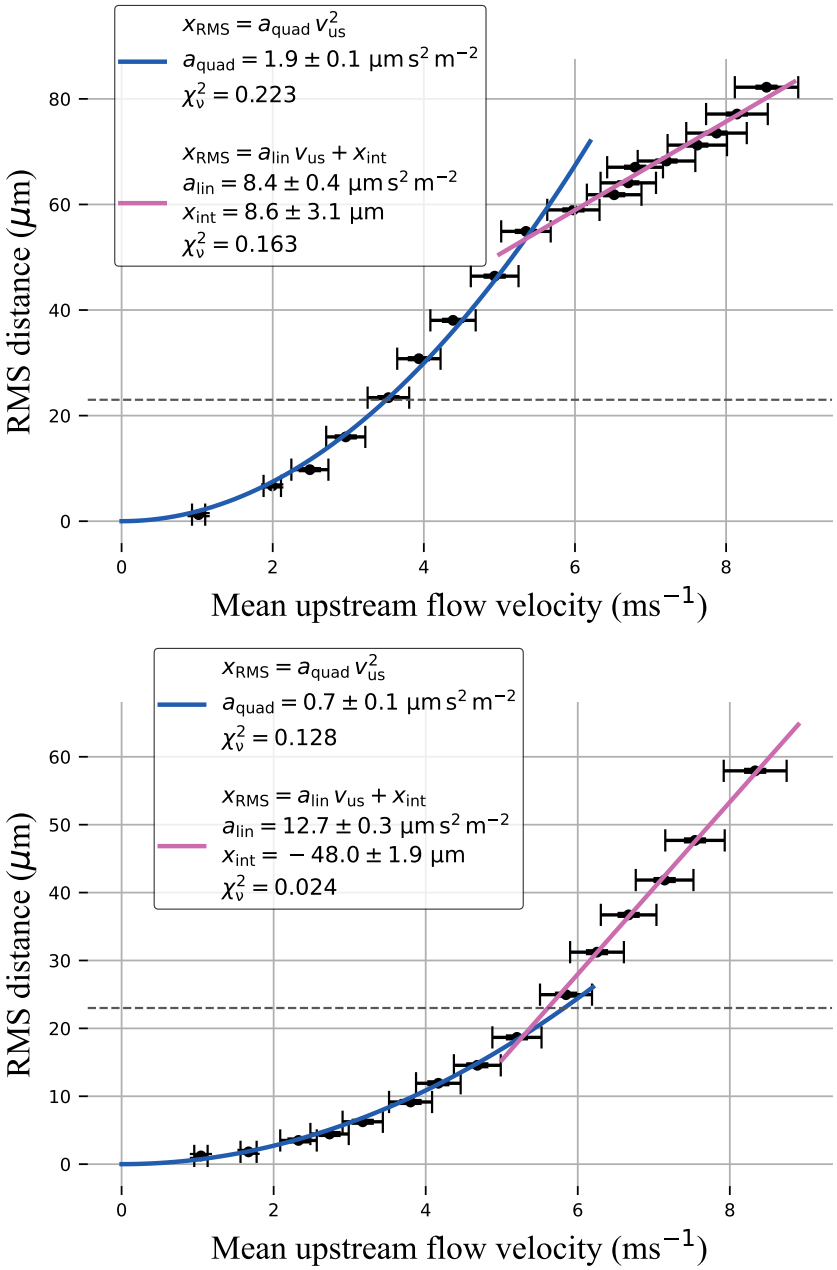

Figure 4.5: RMS displacement as a function of upstream velocity v_{us} for the polyimide ladder (top) and carbon-fibre ladder (bottom), measured at their centres. A quadratic fit is applied below $5.3\,m\,s^{-1}$ and a linear fit above. In both cases, the reduced χ_ν^2 is small, likely due to the limited accuracy of the hot-wire anemometer.

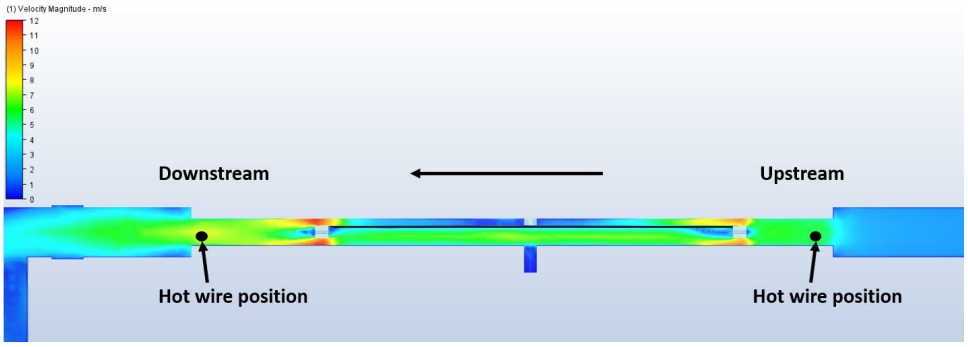

Figure 4.6: CFD simulation of the airflow setup at the University of Oxford using a boundary condition corresponding to a fan flow velocity of $4\,\mathrm{m\,s^{-1}}$. The colour scale shows the magnitude of the airflow velocity.

surement point is approximately $6\,\mathrm{m\,s^{-1}}$, while the corresponding downstream velocity is about $8\,\mathrm{m\,s^{-1}}$. These values are consistent with the previously observed upstream–downstream comparison. The highest velocities occur downstream of the ladder, near the clamp positions, reaching velocities of up to $12\,\mathrm{m\,s^{-1}}$.

4.3 Analysis

In this section, the measured results and CFD simulation of the airflow setup at the University of Oxford are compared with the CFD analysis of the Mu3e pixel detector. An upper limit for the x_{RMS} at the ladder centre is determined, followed by a discussion of its plausibility in the context of the flow regime in which the experiments were conducted.

4.3.1 Expected displacement due to cooling flow

An extensive CFD simulation of the Mu3e pixel detector was carried out by another student working on Mu3e as part of their master's project [51]. The simulated optimised mid-plane velocities of a cooling flow between Layer 3 and Layer 4 are shown in Figure 4.7, while a cross-sectional view is presented in Figure 4.8.

This simulation employs the older "v-fold" design of the polyimide ladder and a different helium distribution, supplying only $13.3\,\mathrm{g\,s^{-1}}$ of helium compared with $16\,\mathrm{g\,s^{-1}}$ in the current design. The maximum helium velocity across the entire mid-plane is $v_{\mathrm{max}} = 21.3\,\mathrm{m\,s^{-1}}$. Assuming density scaling as described in Section 2.3.2, this corresponds to an equivalent airflow velocity of $v_{\mathrm{max,lin}} = 3.7\,\mathrm{m\,s^{-1}}$ under linear velocity scaling, or $v_{\mathrm{max,quad}} = 8.1\,\mathrm{m\,s^{-1}}$ under quadratic velocity scaling. The conversion is made using the established scaling relations:

$$\frac{x_{\mathrm{RMS}}}{x'_{\mathrm{RMS}}} = 1 \quad \Rightarrow \quad \frac{v}{v'} = \left(\frac{\rho'}{\rho}\right)^{\frac{1}{n}}, \tag{4.1}$$

where $n = 1$ for the linear fit or $n = 2$ for the quadratic fit, as motivated in Figure 4.5. Literature values were used for the densities [52, 53].

The converted mid-plane velocity can be compared qualitatively with the upstream velocity in our airflow setup to deduce the expected RMS displacement. For $v_{\mathrm{max,lin}} = 3.7\,\mathrm{m\,s^{-1}}$ the simulated upstream velocity is $v^{us}_{\mathrm{max,lin}} = 4.1\,\mathrm{m\,s^{-1}}$, which yields

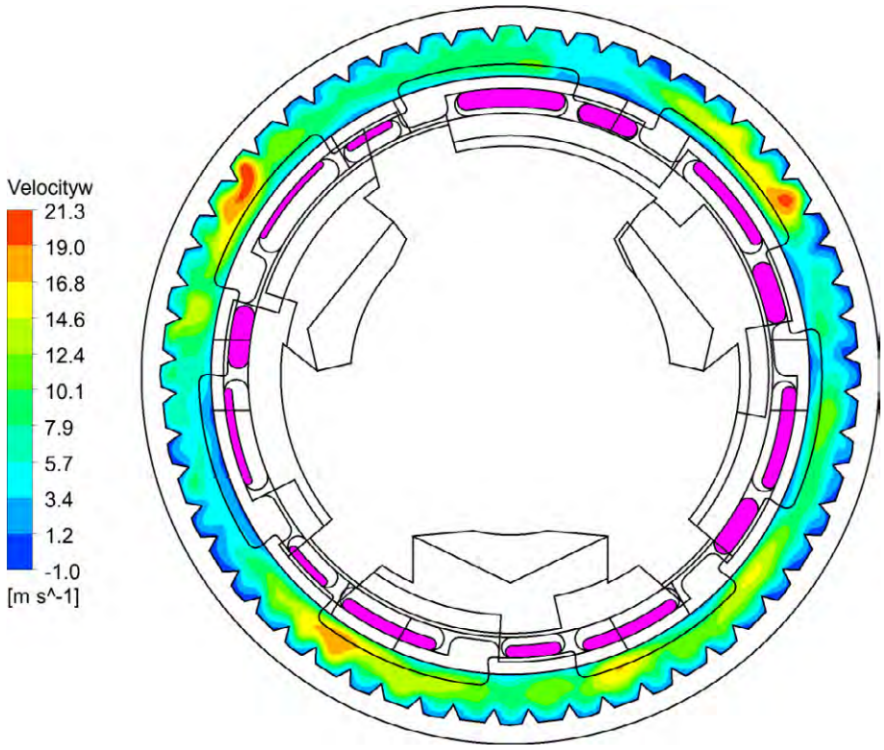

Figure 4.7: Mid-plane velocity distribution across the gap flow between Layer 3 and Layer 4, using the earlier v-fold design [51].

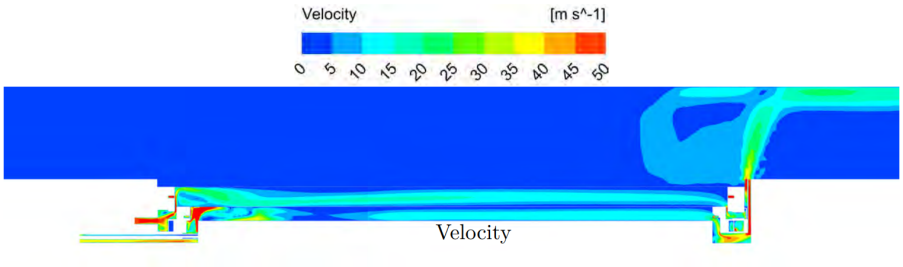

Figure 4.8: Cross-sectional view of the gap flows between SciFi, Layer 3 and Layer 4 [51].

$x_{\mathrm{RMS}} = 11\,\mu\mathrm{m}$ for the carbon-fibre ladder and $x_{\mathrm{RMS}} = 31\,\mu\mathrm{m}$ for the polyimide ladder. For the quadratic fit, the simulated upstream velocity is $v^{us}_{\mathrm{max,quad}} = 8.2\,\mathrm{m\,s^{-1}}$, resulting in $x_{\mathrm{RMS}} = 56\,\mu\mathrm{m}$ for the carbon-fibre ladder and $x_{\mathrm{RMS}} = 78\,\mu\mathrm{m}$ for the polyimide design.

For lower helium velocities, which occur more frequently in the gap geometry, such as $v_{\mathrm{He}} = 14\,\mathrm{m\,s^{-1}}$ observed in the cross-sectional view, the corresponding airflow velocity is $v_{\mathrm{Air}} = 5.4\,\mathrm{m\,s^{-1}}$. This implies an upstream velocity of $v^{\mathrm{us}}_{\mathrm{Air}} = 5.6\,\mathrm{m\,s^{-1}}$, leading to an expected RMS displacement of $x_{\mathrm{RMS}} = 21\,\mu\mathrm{m}$ for the carbon-fibre ladder and $x_{\mathrm{RMS}} = 58\,\mu\mathrm{m}$ for the polyimide ladder. In this case, only the quadratic scaling was considered, since it remains valid up to $v_{\mathrm{Air}} = 5.6\,\mathrm{m\,s^{-1}}$, as shown in Figure 4.9.

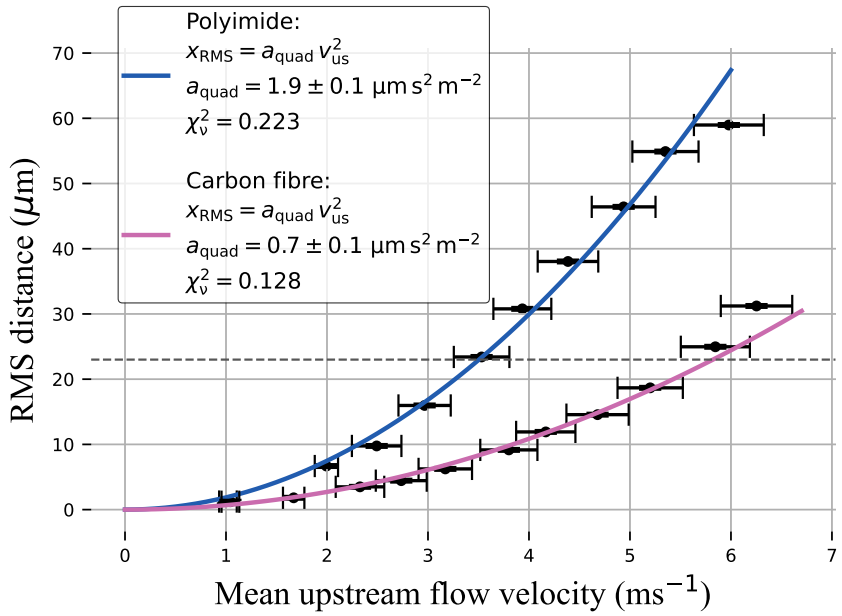

Figure 4.9: Direct comparison of cooling flow induced RMS displacement for the carbon-fibre and polyimide ladder, measured at their centres, at flow velocities below $6\,\mathrm{m\,s^{-1}}$.

4.3.2 Flow regime comparison between simulations

The above comparison is valid only if both experiments operate within the turbulent regime. Outside this regime, dominant excitation mechanisms are determined primarily by geometry and the scaling behaviour is no longer comparable. A quick comparison of the Reynolds numbers shows that this condition is not met.

For the wind tunnel setup, the single ladder and the bottom of the tube housing it can be approximated as two parallel plates. In this case, the characteristic length L is given by the hydraulic diameter,

$$D_h = \frac{4ah}{2a} = 2h. \tag{4.2}$$

Substituting the remaining parameters yields

$$R(U_\infty) = 1677 \cdot U_\infty. \tag{4.3}$$

This configuration corresponds to plane Poiseuille flow, for which the critical Reynolds number, marking the onset of the transitional regime where the flow is no longer laminar, is $Re_{\text{crit}} = 2680$ [54]. The turbulent regime begins at $Re > 5000$, meaning that the wind tunnel operates in the turbulent regime for mid-plane velocities above $3.0\,\text{m}\,\text{s}^{-1}$, corresponding to upstream velocities above $3.4\,\text{m}\,\text{s}^{-1}$.

For the Mu3e setup, the flow can be approximated as annular, with a hydraulic diameter of

$$D_h = 2(r_o - r_i), \tag{4.4}$$

where r_o is the outer radius and r_i the inner radius, as given in Table 1.1. Using helium, which has approximately one-seventh the density of air, this gives

$$R(v_m) = 226 \cdot v_m. \tag{4.5}$$

The critical Reynolds number in the case of an annular flow depends on the ratio of the radii making up the annulus. For a ratio of $k = 0.86$ present in the Mu3e outer layers the critical Reynolds number is $Re_{crit} = 2300$ [54]. Therefore, given v_{mean} =$10\,\text{m}\,\text{s}^{-1}$ the mean flow rate of the experiment, the global flow is considered to be at the boundary between laminar and turbulent flow.

Boundary layer behaviour can also be considered. For an airflow velocity of $10\,\text{m}\,\text{s}^{-1}$,

$$Re_x^{Air} = 6.7 \cdot 10^5 x. \tag{4.6}$$

The transition threshold is often quoted to be at $Re_x \approx 5 \cdot 10^5$. For the longest ladder (Layer 4, $x = 37\,\text{cm}$), this gives $Re_x^{Air} = 2.5 \cdot 10^5$. Thus, both the air and helium boundary layers remain laminar.

4.4 Discussion

A direct comparison between the measurements and CFD simulation conducted at the University of Oxford and the CFD simulation of the Mu3e pixel detector cannot be made directly for several reasons. Firstly, the Mu3e simulation uses an older design with different helium mass flow and ladder geometry. Although a newer CFD study was carried out within the Mu3e collaboration, most of the files were lost or corrupted; despite multiple recovery attempts, the dataset could not be restored. Secondly, it is highly likely that the two setups operate in different flow regimes. While considerable effort was invested in designing the custom tube and clamps to reproduce the experimental boundary conditions, the Reynolds-number matching was not ensured. As a result, the excitation SDs differ between the systems. This mismatch severely constrains the comparability of the results and limits the conclusions that can be drawn.

It should be noted that the Reynolds numbers discussed above describe ideal plane Poiseuille flow and ideal annulus geometry. In both experiments, these idealised conditions are not met. The detector modules have sharp edges with short overlapping segments, and the inlet flow exhibits high velocities that could cause shear layer separation or reduce the Reynolds number at which turbulence develops. The only reliable way to quantify the vibrational behaviour induced by the cooling flow would be to study the actual outer layer or a mock-up replicating it. Unfortunately, no such mock-up was available. Therefore, we adopt $x_{\text{RMS}} = 21\,\mu\text{m}$ as an uppermost limit for the RMS displacement of the carbon-fibre ladder, bearing in mind that this value was obtained in a different setup, likely operating in another flow regime, using a ladder with a partially detached stiffener.

While this value appears large, compared to the intrinsic pixel resolution, its impact is small relative to multiple scattering. For vertex fitting, the multiple scattering uncertainty, σ_{MS}, is about four times larger than the intrinsic pixel uncertainty, σ_l [27]. Including vibrational contributions, the combined uncertainty in the vertical direction increases from $\sigma_z = 20\,\mu\text{m}$ to $\sigma_{z'} = 29\,\mu\text{m}$. This value is comparable to the pixel resolution $\sigma_l = 23\,\mu\text{m}$. Assuming that the vertical uncertainty contributes equally to (or not substantially more than) the in-plane resolution and that ladders combined into modules behave similarly to single ladders, the dominant contribution remains multiple scattering. Vibrations are therefore not expected to significantly degrade the vertex resolution and, by extension, the momentum resolution. A dedicated study would nonetheless be required to confirm the latter.

Chapter 5

Conclusion

The research presented in this manuscript set out to estimate the vibrational behaviour of the Mu3e Layer 4 outer pixel ladder, compare various design configurations, and determine whether additional mechanical stability is required to achieve the target resolution goals of the experiment. The findings indicate that the current design provides sufficient stability: the RMS displacement due to background motion is expected to remain below 3 µm and below 21 µm for vibrations caused by gaseous cooling flow. While the precise impact on track resolution cannot be quantified without dedicated simulations, these values are smaller than the pixel resolution, which is already a minor contributor compared to the effects of multiple scattering.

The reported RMS displacement values should be interpreted with caution, as their estimation relies on several assumptions and is subject to limitations. In particular, differences between the airflow setup and the operational environment, large uncertainties in airflow velocity measurements, and potential differences between the vibrational behaviour of ladders assembled into modules and isolated ladders contribute to these constraints. These examples highlight only some of the limitations encountered in this study.

If further certainty is desired regarding cooling induced vibrations, particularly to exclude any geometrical features that might induce high amplitude oscillations, the most effective approach would be to measure a representative mock-up under the correct helium mass flow. Should greater stability become necessary, increased structural tension has been identified as a promising route. Given the results obtained, however, no further work on this topic seems to be required at this stage.

Appendix A

CAD material tables

Isotropic material	**Al**	**PI**	**Epoxy**	**Cu**
Density	$2710\,\mathrm{kg\,m^{-3}}$	$1420\,\mathrm{kg\,m^{-3}}$	$1300\,\mathrm{kg\,m^{-3}}$	$8960\,\mathrm{kg\,m^{-3}}$
Young's modulus	71 GPa	3 GPa	2 GPa	130 GPa
Shear modulus	26 GPa	1 GPa	1 GPa	49 GPa
Poisson ratio	0.33	0.34	0.37	0.34

Table A.1: Engineering constants for the isotropic materials used for the FEA: aluminium [55], polyimide film [56], epoxy glue [57], and copper [58].

Anisotropic material	**Si**	**Carbon fibre**
Density	$2710\,\mathrm{kg\,m^{-3}}$	$1526\,\mathrm{kg\,m^{-3}}$
Young's modulus E_1	169 GPa	102 GPa
Young's modulus E_2	130 GPa	5 GPa
Young's modulus E_3	130 GPa	5 GPa
Shear modulus G_{12}	51 GPa	2 GPa
Shear modulus G_{13}	51 GPa	2 GPa
Shear modulus G_{23}	80 GPa	2 GPa
Poisson ratio ν_{12}	0.064	0.27
Poisson ratio ν_{13}	0.064	0.27
Poisson ratio ν_{23}	0.36	0.34

Table A.2: Engineering constants for the anisotropic materials used for the FEA. Silicon values are taken from [59], while carbon-fibre values are taken from internal documents.

Composite material	**HDI**	**Interposer flex**
Density	$1841\,\mathrm{kg\,m^{-3}}$	$3865\,\mathrm{kg\,m^{-3}}$
Young's modulus E_1	26 GPa	18 GPa
Young's modulus E_2	4 GPa	2 GPa
Young's modulus E_3	4 GPa	2 GPa
Shear modulus G_{12}	9 GPa	7 GPa
Shear modulus G_{13}	9 GPa	7 GPa
Shear modulus G_{23}	1 GPa	1 GPa
Poisson ratio ν_{12}	0.34	0.35
Poisson ratio ν_{13}	0.34	0.35
Poisson ratio ν_{23}	0.34	0.35

Table A.3: Engineering constants for the composite materials used for the FEA. The given values were calculated using the Reuss or Voigt model depending on spatial orientation.

Appendix B

Additional material

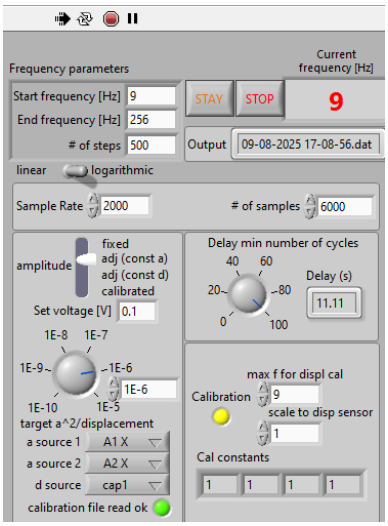

Figure B.1: Photograph of the LabVIEW interface control panel used to set experimental parameters and initiate measurements.

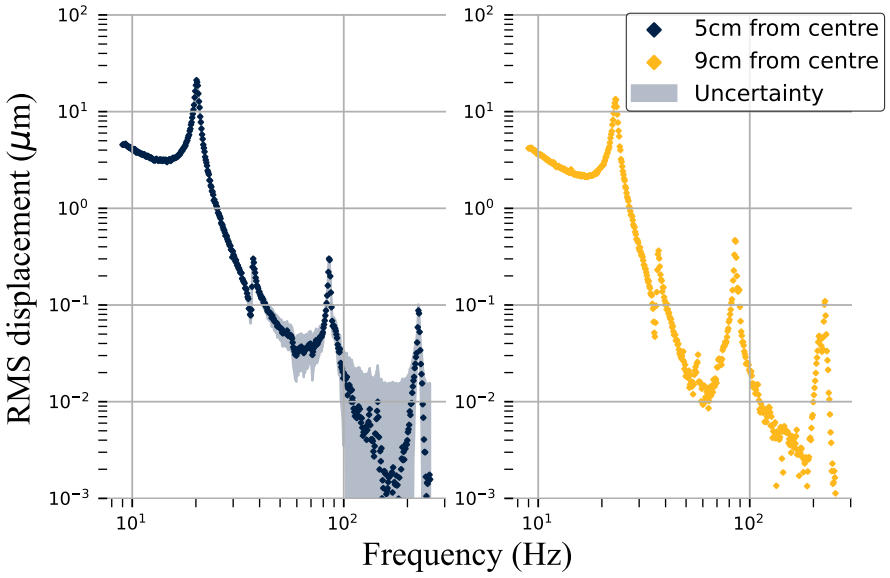

Figure B.2: RMS displacement as a function of excitation frequency of the polyimide ladder at difference distances from the centre. 5 cm from the centre in the left plot and 9 cm from the centre in the right plot.

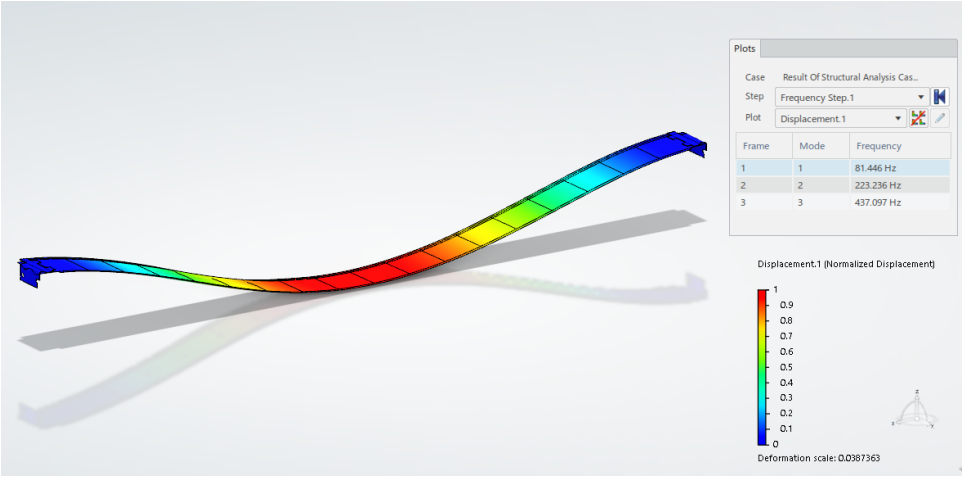

Figure B.3: Simulated first mode of the carbon-fibre ladder with extended stiffener. The frequencies of the first three modes are shown in the "Plots" window.

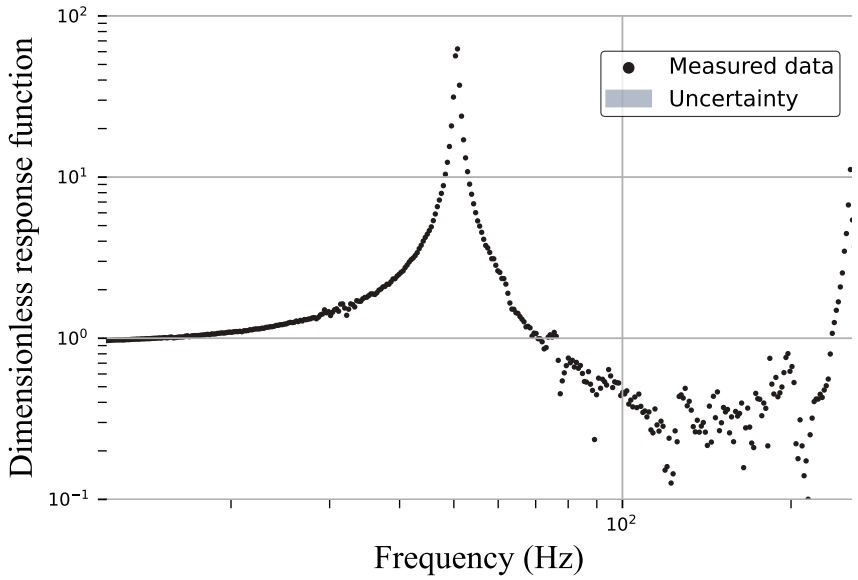

Figure B.4: Unitless response function of the carbon-fibre ladder with a 60 µm stiffener, measured at its centre.

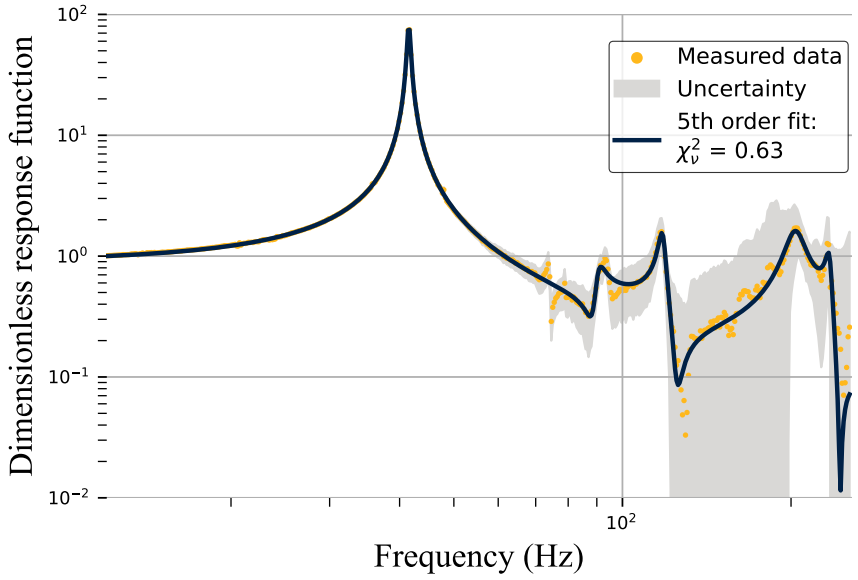

Figure B.5: Linear response function of the carbon-fibre ladder at an off centre position. The response function has been fit with a 5th-order model. The reduced χ^2_ν value is displayed in the legend. The uncertainties are given as a shaded band.

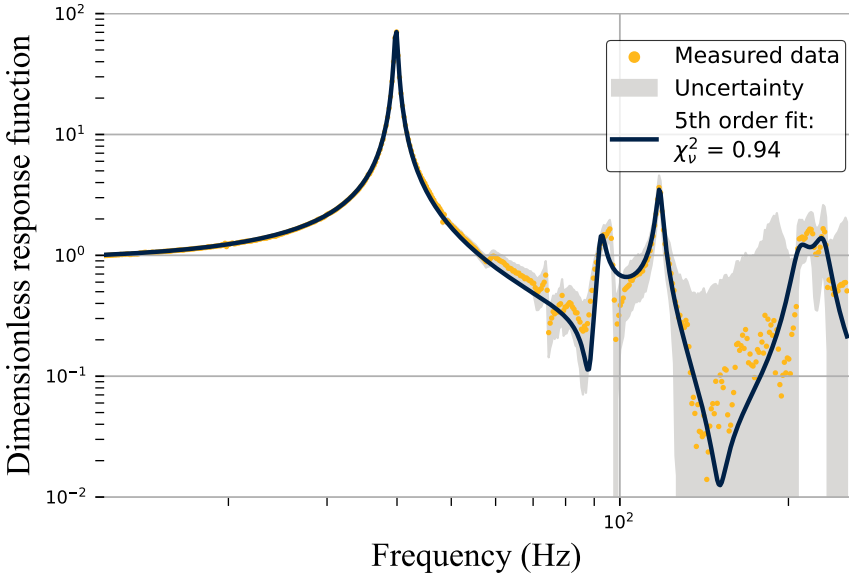

Figure B.6: Linear response function of the carbon-fibre ladder at an off centre position. The response function has been fit with a 5th-order model. The reduced χ^2_ν value is displayed in the legend. The uncertainties are given as a shaded band.

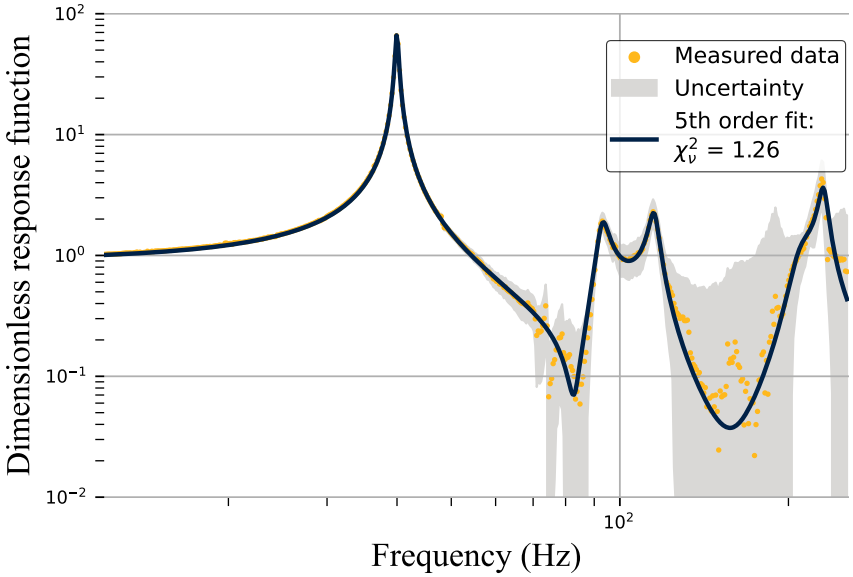

Figure B.7: Linear response function of the carbon-fibre ladder at an off centre position. The response function has been fit with a 5th-order model. The reduced χ^2_ν value is displayed in the legend. The uncertainties are given as a shaded band.

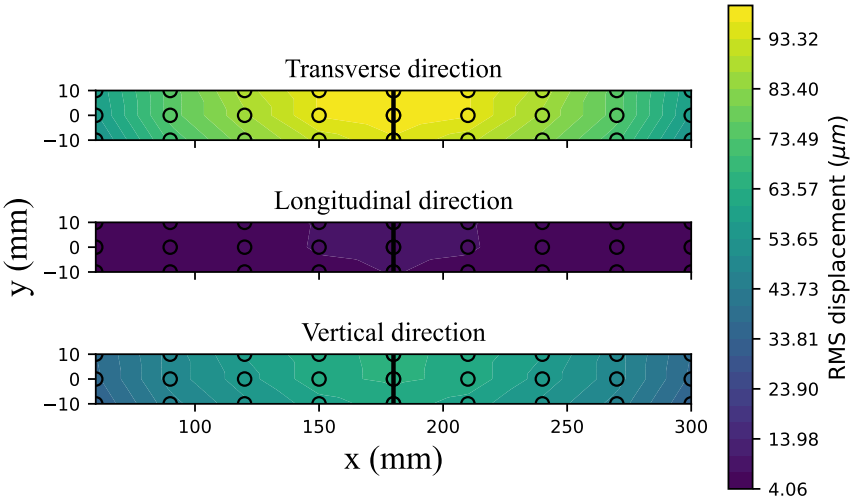

Figure B.8: Predicted RMS displacement of a hypothetical ladder with a first mode frequency of 100 Hz and the same quality factor as the current carbon-fibre ladder measured on the shaker table. The model used is a HO model.

Bibliography

[1] **Particle Data Group** Collaboration, S. Navas *et al.*, "Review of particle physics," *Phys. Rev. D* **110** no. 3, (2024) 030001.

[2] G. Hernández-Tomé, G. López Castro, and P. Roig, "Flavor violating leptonic decays of τ and μ leptons in the standard model with massive neutrinos," *European Physical Journal C* **79** no. 1, (2019) 84.

[3] G. S. Lorenzo Calibbi, "Charged lepton flavour violation: An experimental and theoretical introduction," *La Rivista del Nuovo Cimento* **41** no. 2, (Jan., 2018) 71–174.

[4] S. Weinberg, "The making of the standard model," *The European Physical Journal C-Particles and Fields* **34** (2004) 5–13.

[5] S. Weinberg, *Relativistic Quantum Mechanics*, p. 49–106. Cambridge University Press, 1995.

[6] S. Weinberg, *QUANTUM FIELDS AND ANTIPARTICLES*, p. 191–258. Cambridge University Press, 1995.

[7] V. I. Borodulin, R. N. Rogalyov, and S. R. Slabospitskii, "Core 3.2 (compendium of relations, version 3.2)," 2022. https://arxiv.org/abs/1702.08246.

[8] M. Srednicki, *Representations of the Lorentz group (2)*, p. 205–208. Cambridge University Press, 2007.

[9] Izaak Neutelings, "Standard model,". https://tikz.net/sm_particles/. Accessed: 2025-05-21.

[10] **MuLan Collaboration** Collaboration, T. et al., "Detailed report of the mulan measurement of the positive muon lifetime and determination of the fermi constant," *Phys. Rev. D* **87** (Mar, 2013) 052003.

[11] Santhosh Kumar D, "How neutrinos are formed and detected,". https://digitash.com/science/physics/how-neutrinos-are-formed-and-detected-quantum-mechanics/. Accessed: 2025-05-21.

[12] M. Gonzalez-Garcia and M. Maltoni, "Phenomenology with massive neutrinos," *Physics Reports* **460** no. 1–3, (Apr., 2008) 1–129.

[13] A. de Gouvêa, "(charged) lepton flavor violation," *Nuclear Physics B - Proceedings Supplements* **188** (2009) 303–308. https://www.sciencedirect.com/science/article/pii/S0920563209001716. Proceedings of the Neutrino Oscillation Workshop.

[14] S. T. Petcov, "The Processes $\mu \to e + \gamma, \mu \to e + \overline{e}, \nu' \to \nu + \gamma$ in the Weinberg-Salam Model with Neutrino Mixing," *Sov. J. Nucl. Phys.* **25** (1977) 340. [Erratum: Sov.J.Nucl.Phys. 25, 698 (1977), Erratum: Yad.Fiz. 25, 1336 (1977)].

[15] W. Marciano and A. Sanda, "Exotic decays of the muon and heavy leptons in gauge theories," *Physics Letters B* **67** no. 3, (1977) 303–305. https://www.sciencedirect.com/science/article/pii/037026937790377X.

[16] W. B. et al., "Search for the decay $\mu^+ \to e^+e^+e^-$," *Nuclear Physics B* **260** no. 1, (1985) 1–31.

[17] Paul Scherrer Institute, "Himb (high-intensity muon beams),". https://www.psi.ch/en/impact/himb. Accessed: 2025-08-07.

[18] Paul Scherrer Institute, "The mu3e experiment." https://www.psi.ch/en/mu3e/the-mu3e-experiment. Accessed: 2025-07-28.

[19] K. A. et al., "Technical design of the phase i mu3e experiment," *Nuclear Instruments and Methods in Physics Research Section A: Accelerators, Spectrometers, Detectors and Associated Equipment* **1014** (2021) 165679.

[20] Z. Drasal and W. Riegler, "An extension of the gluckstern formulae for multiple scattering: Analytic expressions for track parameter resolution using optimum weights," *Nuclear Instruments and Methods in Physics Research Section A: Accelerators, Spectrometers, Detectors and Associated Equipment* **910** (Dec., 2018) 127–132.

[21] Robert Bosch Semiconductor LLC, "Welcome to bosch in roseville." https://www.bosch-semiconductors.com/roseville/. Accessed: 2025-08-26.

[22] T. T. Rudzki, *The Mu3e vertex detector – construction, cooling, and first prototype operation*. Phd thesis, Heidelberg University, 2023. Available via heiDOK: https://doi.org/10.11588/heidok.00031602.

[23] U. B. Hartenstein, *Track Based Alignment for the Mu3e Pixel Detector*. PhD thesis, Mainz U., 2019.

[24] C. Kleinwort, "H1 alignment experience," in *Proceedings of the First LHC Detector Alignment Workshop*, A. Bernstein, I. Bloch, E. Duchovni, and et al., eds., pp. 41–50. CERN, 2007. https://cds.cern.ch/record/970621/files/CERN-2007-004.pdf.

[25] M. Weber, "Calibration, alignment and tracking performance of the cms silicon strip tracker," *Nuclear Instruments and Methods in Physics Research Section A: Accelerators, Spectrometers, Detectors and Associated Equipment* **628** no. 1, (2011) 59–63. VCI 2010.

[26] C. Kleinwort and F. Meier, "Alignment of the cms silicon tracker – and how to improve detectors in the future," *Nuclear Instruments and Methods in Physics Research Section A: Accelerators, Spectrometers, Detectors and Associated Equipment* **650** no. 1, (2011) 240–244. International Workshop on Semiconductor Pixel Detectors for Particles and Imaging 2010.

[27] A. Loreti, "Vertex fitting in low-material budget pixel detectors," 2024. https://arxiv.org/abs/2401.13538.

[28] N. Berger, A. Kozlinskiy, M. Kiehn, and A. Schöning, "A new three-dimensional track fit with multiple scattering," *Nuclear Instruments and Methods in Physics Research Section A: Accelerators, Spectrometers, Detectors and Associated Equipment* **844** (Feb., 2017) 135–140.

[29] A. Schöning, "A general track fit based on triplets," 2025. https://arxiv.org/abs/2406.05240.

[30] P. Stoica and R. L. Moses, *Spectral Analysis of Signals*. PearsonPrentice Hall, Upper Saddle River, NJ, 1 ed., 2005. https://user.it.uu.se/~ps/SAS-new.pdf.

[31] A. Birolini, *Reliability Engineering: Theory and Practice*. Springer Science & Business Media, Berlin and New York, 5 ed., 2007. https://link.springer.com/book/10.1007/978-3-662-54209-5.

[32] N. Wiener, "Generalized harmonic analysis," *Acta Mathematica* **55** (1930) 117–258.

[33] J. W. M. Bush, "Surface tension module." Department of mathematics, massachusetts institute of technology, n.d. https://web.mit.edu/1.63/www/Lec-notes/Surfacetension/Lecture1.pdf.

[34] H. Schlichting and K. Gersten, *Boundary-Layer Theory*. Springer Berlin Heidelberg, 2016. https://books.google.co.uk/books?id=bOUyDQAAQBAJ.

[35] L. J. Clancy, *Aerodynamics*. John Wiley & Sons, Hoboken, NJ, 1975.

[36] F. Russo and N. T. Basse, "Scaling of turbulence intensity for low-speed flow in smooth pipes," *Flow Measurement and Instrumentation* **52** (2016) 101–114.

[37] Siemens Digital Industries Software, "Vibration Shaker Table Considerations." https://community.sw.siemens.com/s/article/Vibration-Shaker-Table-Considerations. Accessed 4 August 2025.

[38] KEMET Electronics Corporation, "AE035035D18H18DF – Resin Coated Multilayer Piezoelectric Actuator." https://search.kemet.com/component-documentation/download/specsheet/AE035035D18H18DF. Datasheet, retrieved 2025-08-13.

[39] Micro-Epsilon, "capancdt 6110: Capacitive displacement measurement system." https://www.micro-epsilon.com/fileadmin/download/excerpts/dax--capaNCDT-611x--en.pdf. Accessed: 2025-07-29.

[40] National Instruments, *LabVIEW*. National Instruments, Austin, Texas. https://www.ni.com/labview. System Design Software.

[41] C. E. Shannon, "Communication in the presence of noise," *Proceedings of the IRE* **37** (1949) 10–21. https://api.semanticscholar.org/CorpusID:12037187.

[42] T. Ikeda, *Fundamentals of Piezoelectricity*. Oxford science publications. Oxford University Press, 1996. https://books.google.ch/books?id=TrFvQgAACAAJ.

[43] J. C. for Guides in Metrology, "Jcgm 100:2008 – evaluation of measurement data: Guide to the expression of uncertainty in measurement," tech. rep., Joint Committee for Guides in Metrology (JCGM), 2008. Also known as the GUM, freely available from the BIPM.

[44] Dassault Systèmes, "Scenario Creation App." https://www.3ds.com. Software used via the 3DEXPERIENCE platform.

[45] W. Voigt, "Ueber die beziehung zwischen den beiden elasticitätsconstanten isotroper körper," *Annalen der Physik* **274** no. 12, (1889) 573–587.

[46] A. Reuss, "Berechnung der fließgrenze von mischkristallen auf grund der plastizitätsbedingung für einkristalle .," *ZAMM - Journal of Applied Mathematics and Mechanics / Zeitschrift für Angewandte Mathematik und Mechanik* **9** no. 1, (1929) 49–58.

[47] P. D. Welch, "The use of fast fourier transform for the estimation of power spectra: A method based on time averaging over short, modified periodograms," *IEEE Transactions on Audio and Electroacoustics* **15** (1967) 70–73. https://api.semanticscholar.org/CorpusID:13900622.

[48] A. Savitzky and M. J. E. Golay, "Smoothing and differentiation of data by simplified least squares procedures," *Analytical Chemistry* **36** no. 8, (1964) 1627–1639.

[49] Testo SE&Co.KGaA, "Testo405i Thermal Anemometer with Smartphone Operation (model05601405)." Online. https://www.testo.com/en-MY/testo-405i/p/0560-1405. Accessed: 2025-08-05.

[50] Autodesk Inc., "Autodesk CFD — Computational Fluid Dynamics Software." https://www.autodesk.com/au/products/cfd/overview. Accessed: 2025-08-05.

[51] M. Deflorin, "Helium cooling of silicon pixel detector for mu3e experiment," Master's thesis, University of Applied Sciences and Arts Northwestern Switzerland (FHNW), Institute of Thermal and Fluid Engineering (ITFE), March, 2019. https://www.psi.ch/sites/default/files/import/mu3e/ThesesEN/MasterDeflorin.pdf.

[52] E. Torenbeek, "Appendix b: International standard atmosphere," in *Advanced Aircraft Design: Conceptual Design, Analysis and Optimization of Subsonic Civil Airplanes*, E. Torenbeek, ed., pp. 397–398. John Wiley & Sons, Ltd., 2013. Appendix B contains the International Standard Atmosphere table.

[53] Periodic-Table.org, "Helium – density." https://www.periodic-table.org/helium-density/. Accessed 2025-08-17.

[54] H.-S. Dou, B. C. Khoo, and H. M. Tsai, "Determining the critical condition for turbulent transition in a full-developed annulus flow," *Journal of Petroleum Science and Engineering* **73** no. 1, (2010) 41–47.

[55] thyssenkrupp Materials (UK) Ltd, "Information on Aluminium 1050." https://www.thyssenkrupp-materials.co.uk/aluminium-1050.html. Accessed: 2025-08-08.

[56] DuPont Electronics & Imaging, "Kapton: Summary of Properties (Document EI-10142)." https://www.dupont.com/content/dam/electronics/amer/us/en/electronics/public/documents/en/EI-10142_Kapton-Summary-of-Properties.pdf. Accessed: 2025-08-08.

[57] Z. Jia, D. Hui, G. Yuan, J. Lair, K. tak Lau, and F. Xu, "Mechanical properties of an epoxy-based adhesive under high strain rate loadings at low temperature environment," *Composites Part B: Engineering* **105** (2016) 132–137.

[58] MIT Department of Materials Science and Engineering, "Copper: Material Properties." https://www.mit.edu/~6.777/matprops/copper.htm. Accessed: 2025-08-08.

[59] M. A. Hopcroft, "The young's modulus of silicon." https://siliconmodulus.com/. Accessed: 2025-08-08.

ETH

Eidgenössische Technische Hochschule Zürich
Swiss Federal Institute of Technology Zurich

Eigenständigkeitserklärung

Die unterzeichnete Eigenständigkeitserklärung ist Bestandteil jeder während des Studiums verfassten schriftlichen Arbeit. Eine der folgenden zwei Optionen ist **in Absprache mit der verantwortlichen Betreuungsperson** verbindlich auszuwählen:

☐ Ich erkläre hiermit, dass ich die vorliegende Arbeit eigenverantwortlich verfasst habe, namentlich, dass mir niemand beim Verfassen der Arbeit geholfen hat. Davon ausgenommen sind sprachliche und inhaltliche Korrekturvorschläge der Betreuungsperson. Es wurden keine Technologien der generativen künstlichen Intelligenz[1] verwendet.

☒ Ich erkläre hiermit, dass ich die vorliegende Arbeit eigenverantwortlich verfasst habe. Dabei habe ich nur die erlaubten Hilfsmittel verwendet, darunter sprachliche und inhaltliche Korrekturvorschläge der Betreuungsperson sowie Technologien der generativen künstlichen Intelligenz. Deren Einsatz und Kennzeichnung ist mit der Betreuungsperson abgesprochen.

Titel der Arbeit:

Vibrations of Ultralight Tracking Detector Structures

Verfasst von:
Bei Gruppenarbeiten sind die Namen aller Verfasserinnen und Verfasser erforderlich.

Name(n):	**Vorname(n):**
Moretti	Mattia

Ich bestätige mit meiner Unterschrift:
- Ich habe mich an die Regeln des «Zitierleitfadens» gehalten.
- Ich habe alle Methoden, Daten und Arbeitsabläufe wahrheitsgetreu und vollständig dokumentiert.
- Ich habe alle Personen erwähnt, welche die Arbeit wesentlich unterstützt haben.

Ich nehme zur Kenntnis, dass die Arbeit mit elektronischen Hilfsmitteln auf Eigenständigkeit überprüft werden kann.

Ort, Datum	**Unterschrift(en)**
Zürich, 08.09.2025	mattia

Bei Gruppenarbeiten sind die Namen aller Verfasserinnen und Verfasser erforderlich. Durch die Unterschriften bürgen sie grundsätzlich gemeinsam für den gesamten Inhalt dieser schriftlichen Arbeit.

[1] Für weitere Informationen konsultieren Sie bitte die Webseiten der ETH Zürich, bspw. https://ethz.ch/de/die-eth-zuerich/lehre/ai-in-education.html und https://library.ethz.ch/forschen-und-publizieren/Wissenschaftliches-Schreiben-an-der-ETH-Zuerich.html (Änderungen vorbehalten).